LA-UR-18-22479 (Accepted Manuscript)

Constrained optimization framework for interface-aware sub-scale dynamics models for voids closure in Lagrangian hydrodynamics

Barlow, Andrew
Klima, Matej
Shashkov, Mikhail Jurievich

To be published in: Journal of Computational Physics

DOI to publisher's version: 10.1016/j.jcp.2018.03.034

Permalink to record: http://permalink.lanl.gov/object/view?what=info:lanl-repo/lareport/LA-UR-18-22479

Accepted Manuscript

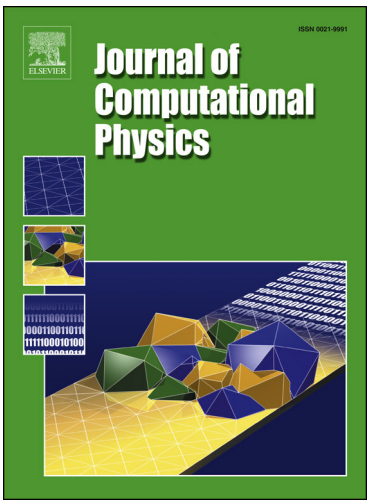

Constrained optimization framework for interface-aware sub-scale dynamics models for voids closure in Lagrangian hydrodynamics

Andrew Barlow, Matej Klima, Mikhail Shashkov

PII: S0021-9991(18)30194-3
DOI: https://doi.org/10.1016/j.jcp.2018.03.034
Reference: YJCPH 7926

To appear in: *Journal of Computational Physics*

Received date: 28 September 2017
Revised date: 26 January 2018
Accepted date: 21 March 2018

Please cite this article in press as: A. Barlow et al., Constrained optimization framework for interface-aware sub-scale dynamics models for voids closure in Lagrangian hydrodynamics, *J. Comput. Phys.* (2018), https://doi.org/10.1016/j.jcp.2018.03.034

Highlights

- Developed the new treatment of voids closure which is used in the Lagrangian stage of our indirect ALE scheme.
- New approach is based on the interface-aware sub-scale-dynamics closure model for multimaterial cells with voids.
- Presented results of the comprehensive testing of the new model for one- and two-dimensional multimaterial calculations in the presence of voids.
- Presented a sneak peek of a realistic shaped charge calculation in the presence of voids and solids.

Journal of Computational Physics (2018)

Contents lists available at ScienceDirect

Journal of Computational Physics

journal homepage: www.elsevier.com/locate/jcp

Constrained optimization framework for interface-aware sub-scale dynamics models for voids closure in Lagrangian hydrodynamics

Andrew Barlow[a], Matej Klima[b,c], Mikhail Shashkov[c,*]

[a] *Computational Physics Group, AWE Aldermaston, Reading, Berkshire, RG7 4PR, UK*
[b] *Faculty of Nuclear Sciences and Physical Engineering, Czech Technical University in Prague, Brehova 7, Praha 1, 115 19, Czech Republic*
[c] *X-Computational Physics, XCP-4, Los Alamos National Laboratory, Los Alamos, NM 87545, USA*

ARTICLE INFO

Article history:

Lagrangian hydrodynamics, multi-material cells, interface-aware sub-scale closure models, void closure.

ABSTRACT

In hydrocodes, voids are used to represent vacuum and model free boundaries between vacuum and real materials. We give a systematic description of a new treatment of void closure in the framework of the multimaterial arbitrary Lagrangian-Eulerian (ALE) methods. This includes a new formulation of the interface-aware sub-scale-dynamics (IA-SSD) closure model for multimaterial cells with voids, which is used in the Lagrangian stage of our indirect ALE scheme.

The results of the comprehensive testing of the new model are presented for one- and two-dimensional multimaterial calculations in the presence of voids. We also present a sneak peek of a realistic shaped charge calculation in the presence of voids and solids.

1. Introduction and rationale

In this paper we consider the class of so-called indirect Arbitrary Lagrangian-Eulerian (ALE) numerical methods [11, 4] in which the solution process is separated into three distinct stages. These are:

1. **Lagrangian stage**, in which the solution and the computational mesh is updated,
2. **Rezoning stage**, in which the nodes of the computational mesh are moved to more optimal positions,
3. **Remapping stage**, in which the Lagrangian solution is conservatively transferred to the rezoned mesh.

*Corresponding author. Tel.: 1-505-667-4400
e-mail: Andy.Barlow@awe.co.uk (Andrew Barlow), klimamat@fjfi.cvut.cz (Matej Klima), shashkov@lanl.gov (Mikhail Shashkov)

In particular, any Eulerian method on an arbitrary mesh can be considered an ALE method if the mesh is always returned to its initial configuration at each rezone stage. This type of Eulerian methods is usually referred to as "Eulerian=Lagrange+Remap".

Multimaterial cells, which may contain several materials, can appear even in pure Lagrangian calculations. This can happen if the initial configuration consists of multiple material regions that have complicated geometric shapes, such that it is hard, or impossible, for a given mesh resolution to create an initial mesh which conforms to the material interfaces.

In many multimaterial problems, the initial mesh can be aligned with a material interface so that each cell of the mesh contains only one material. However, complex high-speed multimaterial flows with strong shear deformations often make it impossible to keep material interfaces aligned with the mesh. ALE methods are therefore currently the only proven technology to solve such problems. In ALE methods, the mesh does not move with the fluid and so it is unavoidable that multimaterial cells containing several materials will appear.

In many real applications one might need to deal not only with real materials, but also with voids. Voids can be considered as a way of representing both internal free boundaries (e.g. cavities, pores) and external free boundaries (expansion in to vacuum). Both Lagrangian and Eulerian hydrocodes encounter difficulties with modeling problems related to expansion in to vacuum [15, 24] and more recent papers [17, 12].

The artificial gas approach

In some codes, voids are modeled as a light and compressible *artificial gas*, often with air-like material properties. Here we will give some arguments why, in our opinion, such an approach may lead to physically wrong results and affect the robustness of the algorithm. We can start by saying that clearly there are no universal gas properties that can be used to represent voids for all problems. And even in a single problem where different materials are in contact with the vacuum, there is no clear recommendations as to how light and how compressible the gas should be.

Let us now consider an example – projectile impact problem, it is critical for such a problem to have an accurate void closure and void opening capability. If one models such an impact problem with both the impactor and the target surrounded by air, some of the air can often be trapped between the two materials as they come together. The air may then end up in a spurious state, which may in turn cause robustness problems. This can also lead to the wrong contact states as the pressure in the air will not match the normal stress between the plates at impact when there is no air present between the plates. For an enclosed cavity the air may stop the materials coming into close contact (e.g. 1D impact of plates separated by gas). The remaining air may reach non-physical states in equation of state (EOS) space, with high sound speeds – e.g. projectile impact problems and collapsing pores filled with air.

Consider a situation where the air remains after an impact. Gases cannot support tension, so how can void opening be detected? And if the materials do open, what will happen to the state of the gas as it is stretched to lower and lower density? Will the gas that was not trapped flow back into the opening to produce the correct gas thermodynamic states or lead to spurious states and sound speeds?

Alternatively, one may think of modeling void opening in isolation either within a material or at an initially closed

material interface. Without introducing voids, from where is the artificial gas going to come from? Adding an arbitrary amount of gas will create mass.

The robustness issue is also important for problems which involve very high deformation. In such situations the artificial gas often has no impact on the physics of the problem, but must be meshed to allow multimaterial ALE to be used to handle the high deformation in the solid materials. If air is used, the air equation of state can get in to spurious high sound speed states very easily, which often cause calculations to fail for many reasons, e.g. mesh tangling, over advection etc.

In addition, the artificial gas representing the void requires EOS calls in the code. Moreover, in ALE methods the artificial gas is treated just like any other real material during the rezoning and remapping stages. These factors both contribute to the overall computational cost.

Treating the space around solid components as voids removes all these robustness issues without degrading the fidelity of the simulation and allows impacts and material opening to be handled accurately and robustly. We are convinced of the importance of developing a void treatment within the framework of Lagrangian and ALE methods, hence, the need for this paper. In this paper we will consider void closure only.

A review of our algorithm

The staggered compatible discretization of Lagrangian hydrodynamics is used in this paper [7, 4]. In this framework the velocity is defined at the nodes of the mesh – it is assumed that all materials have the same velocity (single velocity model) within multimaterial cells. Each material has its own volume, density, specific internal energy and pressure. Void has non-zero volume (that is the volume of the space it occupies), but the rest of the quantities are zero. In the single material case, mass, density, internal energy and pressure are defined in the cells of the mesh. In the case of multimaterial flows, there may be pure cells containing only one material (a real material or void) and multimaterial cells which may contain several real materials and void. In a multimaterial cell, each material (including void) is represented by its pure material polygon (sub-cell). These are obtained by using an interface reconstruction method. In our paper we use the moment-of-fluid (MOF) interface reconstruction method [10, 1] which was recently extended [13] such that it returns not just material polygons but also their connectivity (*mini mesh*), which is needed for our interface-aware closure model.

Multimaterial cells in our ALE method can represent interfaces between real materials as well as free boundary (interfaces of the real materials with vacuum) that can undergo high deformation. The main research concerns are:

- Accurately updating the thermodynamic states of the real individual material components in the multimaterial cell,
- deciding when the void closes,
- determining the nodal forces that the multimaterial zone generates despite the lack of information about the velocity distribution within multimaterial cells.

A *closure model* is then required to close the governing equations, which are otherwise under-determined. Its role is to define how the volume fractions of all the materials (including void) will evolve in time and how the states of the real individual materials evolve during a single Lagrangian step.

The approach described in this paper is based on the IA-SSD concept [3] originally designed for multimaterial flows in which computational cells may contain several real materials. In this paper we introduce special procedures for void closure and extend the IA-SSD approach so that the multimaterial cells can contain voids as well. The IA-SSD closure model for the Lagrangian stage of ALE consists of two stages:

1. ***Bulk* stage** uses the equal compressibility model [6](Section 3.11), [3, 4] or the constant volume fraction model in the case of fluids. In this model, the total change in the volume of the multimaterial cell is distributed between all materials according to the volume fraction that is constant in time. This applies for both real materials and voids, therefore, void cannot close at this stage. This model does not take into account any sub-scale interactions between materials inside the multimaterial cell.
2. ***Sub-scale* stage** takes into account the interactions of the materials inside the multimaterial cell. At this stage, information about the topology of the sub-cells inside the multimaterial cell is utilized, allowing the orientation of internal interfaces to be included in the model. Each material, including void, interacts in a pair-wise fashion with all materials that it shares a common boundary with.

The pair-wise interactions of the real materials and real material and void are based on the solution of the acoustic Riemann problem and are limited using physically justified constraints. Those constraints are:

- Positivity of volume for real material sub-cells,
- non-negativity of volume of void sub-cells,
- positivity of internal energy,
- a controlled rate of pressure relaxation.

The volume of voids can be zero as a result of the sub-scale stage – this indicates that the void has been closed. To determine the values of the limiter coefficients, a constrained-optimization framework is employed using a quadratic objective function with linear constraints.

There is nothing special with the rezone stage for ALE in the presence of voids – all points are moved according to some rezone strategy [4]. Clearly, the choice of the rezone strategy will strongly affect the results of calculations. To make our results reproducible, in all our examples we use the Eulerian=Lagrange+Remap approach in which all points move back to their original positions.

In this paper remapping is performed using the flux form of the intersection-based remap as described in [4], [14]. To make our results reproducible, we use a first-order remap. There is nothing special about the remapping of cells with voids, void just acts as a special "material" with zero density (mass) and zero internal energy. In the first order case, there is nothing special about nodal remap. However, in Section 5 we briefly describe the so-called *kinetic*

energy fix which is needed in the general case to enforce the conservation of total energy. We do not describe any other details of the remapping in this paper and instead we refer the interested reader to [4], [14].

The remainder of the paper is organized as follows. In Section 2 we introduce the notation related to the representation of the materials. The generic description of the Lagrangian stage of ALE is given in Section 3. The sub-scale stage of the closure model is presented in Section 4. Algorithmic choices for the closure model are described and justified in Section 5. Numerical examples are presented in Section 6. Conclusions and a description of future research is provided in Section 7.

2. Notation and the representation of materials

To be consistent with [3] we will use the same notation. The cell (zone) of the mesh is denoted by z and all zonal quantities are identified by the subscript z. For example, V_z represents the volume of the zone. The superscript n is used for identifying quantities at the time level t^n. For example, the volume of the zone z at time t^n is denoted by V_z^n.

The multimaterial zones are identified by the presence of more than one material, real or void. The index i is used to identify specific materials (including void). The volume of the material i in zone z at time t^n is denoted by $V_{z,i}^n$. Each real material has its own mass, $m_{z,i}$; density $\rho_{z,i}^n$; pressure, $p_{z,i}^n$ and internal energy, $\varepsilon_{z,i}^n$. It is useful to introduce the volume fraction for each material, $0 < \alpha_{z,i}^n < 1$.

If a multimaterial cell contains void the index v will be used to distinguish it from the real materials *only* if void is treated in a different way. Void is described by its volume $V_{z,v}^n$ and volume fraction $\alpha_{z,v}^n$. The void density (mass), pressure, speed of sound and internal energy are always zero.

There are also two special types of cell vertices / points. The *void* points are points surrounded by pure void cells only. Points are designated as *real-material* if at least one of the surrounding cells contains at least one real material sub-cell (but voids can be present as well).

3. Generic description of the Lagrangian stage for multimaterial flows

In this section we will give a generic description of the Lagrangian stage in the presence of multimaterial cells with voids. While voids can close, a real material present in the multimaterial cell at time t^n will remain in that cell upon the completion of the Lagrangian step. We will describe the predictor part of the time integration – for full details of time integration, one can refer to [3]. The Lagrangian stage starts with the computation of common pressures in the multimaterial cells

$$\tilde{p}_z^n = \sum_{i \in M(z)} \alpha_{z,i}^n \, p_{z,i}^n \,, \tag{1}$$

where $M(z)$ is the set of all materials in the multimaterial cell, including void material. The common pressure in the single-material cells is just equal to the material pressure and the common pressure in the void cells is zero.

Next,the corner forces in each cell acting on each of the cells points are computed using common zonal pressures.

This allows the new velocities of the *real-material points* to be computed.

The *void points* cannot be moved using the momentum equation because their mass is zero and there are no forces acting on them. This means that the mesh would tangle if only the Lagrangian stage was used. However, the Eulerian = Lagrange + Remap algorithm, which is used in this paper, avoids this situation. For a general ALE method, a special algorithm for the movement of such points at the Lagrangian stage may be necessary.

Next, the coordinates of all *real-material points*, are updated, which allows the new volumes of all zones to be computed. Let us note that the volumes of the pure void cells may also change if at least one of the vertices of the void cell is a real-material point.

Using the new volume we can update the density, specific internal energy and pressure in all the pure cells containing real materials.

For pure void cells we do not need to do anything.

Next, we need to update the densities and specific internal energies for all the real materials in the multimaterial cells. If a void was present in the multimaterial cell at t^n, we also need to decide if it will close. The objective of closure models for multimaterial cells is to answer all these questions. Our closure model is described in the next section.

4. Void Closure Model

In this section, where it does not lead to misunderstanding, the zonal index z is dropped because only a single cell is considered. Additionally, in most cases the time index is also dropped.

Our void closure model consists of two stages - bulk stage and sub-scale stage.

4.1. Bulk Stage

At the bulk stage we use the equal compressibility model, whereby it is assumed that the volume fraction does not change in time, i.e. $\alpha_{z,i}^{n+1} = \alpha_{z,i}^{n}$. At bulk stage, the total change in the volume of the multimaterial cell, ΔV^{n+1}, is distributed between all constituents in the multimaterial cell, including void, proportionally to its volume fraction from the previous time step

$$\Delta V_i^{n+1,bulk} = \alpha_i^n \, \Delta V^{n+1} \, . \tag{2}$$

Therefore, void cannot close at this stage.

The update of density, specific internal energy and pressure for the real materials in the multimaterial cell is the same as described in [3] for the case when the multimaterial cell only contains real materials. In particular the update of the internal energies for each real material is done using individual internal energy equations and expression (2) for the change in the material volume

$$m_i \, (\varepsilon_i^{n+1} - \varepsilon_i^n) = -p_i^n \, \Delta V_i^{n+1,bulk} \, . \tag{3}$$

4.2. Sub-scale Stage

The sub-scale stage takes into account the interactions between the materials inside the multimaterial cell. It is assumed that the topology of the materials inside a multimaterial cell is known from the interface reconstruction algorithm. Each material in the multimaterial cell is represented by a pure sub-polygon. The set of the materials in the multimaterial cell which have a face in common with material i is denoted by $M(i)$. At the sub-scale stage each material, including void, interacts in a pair-wise fashion with all the materials that it shares a common boundary with.

4.2.1. Volume change model

To take into account the difference in pressure of the materials which share the face, the volume exchange between the neighboring materials is introduced in flux form as

$$\Delta V_i = \Delta V_i^{bulk} + \sum_{k \in M(i)} \delta V_{i,k}\,, \quad \delta V_{i,k} = -\delta V_{k,i}\,. \tag{4}$$

The volume exchange term is constructed as follows:

$$\delta V_{i,k} = \Psi_{i,k}\, \delta V_{i,k}^{max}\,, \tag{5}$$

where $\delta V_{i,k}^{max}$ is the maximum allowed volume exchange between adjacent materials, or real material and void, due to the imbalance in pressure, where $0 \le \Psi_{i,k} \le 1$ are the limiters which are chosen in such a way that the overall model does not violate physically justifiable constraints – for example, the positivity of the volume of any real material sub-cell. The obvious requirement $0 \le \Psi_{i,k}$ ensures that the limiter does not reverse the direction of the "physical" force. The definition of the upper bound $\Psi_{i,k} \le 1$ is more questionable, however, it is sensible to not increase the magnitude of the sub-scale fluxes.

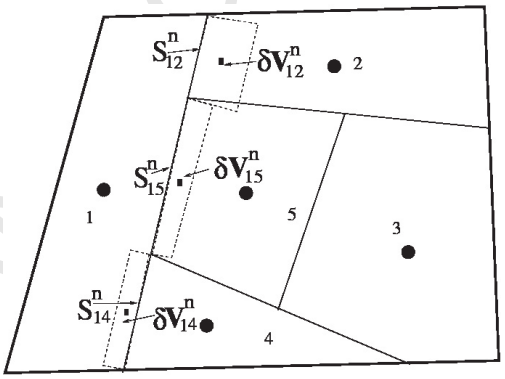

Fig. 1: Multimaterial cell: definition of the relative volume exchange.

The expression for the exchange term $\delta V_{i,k}^{max}$ between real materials is estimated using the acoustic Riemann solver (see [3] for details).

In the case of the volume exchange between real material and void we define $\delta V_{i,v}^{max}$ as follows

$$\delta V_{i,v}^{max} = \frac{p_i}{\rho_i\, c_i}\, S_{i,v}\, \Delta t\,, \tag{6}$$

where c_i is the adiabatic speed of sound in the material i, and $S_{i,v}$ is the area of the interface between materials i and void, see Fig.1.

In Fig.1, a multimaterial cell with five materials is presented with a graphical representation of $\delta V_{i,k}$ (the same notation is used for its volume and the corresponding rectangle). For the material #1 ($i = 1$) there are three neighbors: {2, 4, 5}. In the situation presented p_1 is larger than p_2 and p_5 and smaller than p_4.

Bounds for material volume

Following [3], the following constraints are imposed on the volume of a real material sub-cell:

$$V_i^{n+1} \geq \kappa_{bot}\, V_i^{n+1,bulk}\,, \quad 1 \geq \kappa_{bot} > 0\,. \tag{7}$$

Here, the parameter κ_{bot} controls how close to zero the volume of the real material may reach. In the results presented in this paper κ_{bot} is presumed to be constant in time for all materials. The constraints for real materials (7) represent a system of linear inequalities with respect to the limiters $\Psi_{i,k}$:

$$V_i^{n+1,bulk} + \sum_{k \in M(i)} \Psi_{i,k}\, \delta V_{i,k}^{max} \geq \kappa_{bot}\, V_i^{n+1,bulk}\,. \tag{8}$$

For void, the volume constraint can be expressed as

$$V_v^{n+1} \geq 0\,, \tag{9}$$

that is, void closes if $V_v^{n+1} = 0$ at the end of the subscale stage.

For void, the constraint (9) leads to the following linear inequality (with respect to $\Psi_{i,k}$):

$$V_v^{n+1,bulk} + \sum_{k \in M(v)} \Psi_{v,k}\, \delta V_{v,k}^{max} \geq 0\,. \tag{10}$$

4.2.2. Specific internal energy evolution

In the IA-SSD closure model, each real material has a separate approximate $p\,dV$ equation. In [3] we use the following equation which guarantees the conservation of total energy:

$$m_i \left(\varepsilon_i^{n+1} - \varepsilon_i^n\right) = -p_i^n\, \alpha_i^n\, \Delta V^{n+1} - \sum_{k \in M(i)} p_{i,k}^{*} \Psi_{i,k}\, \delta V_{i,k}^{max}\,, \tag{11}$$

where the pressure $p_{i,k}^{*}$ is obtained from the one-dimensional acoustic Riemann problem between materials i and k.

Since the time of publishing [3], we have found that better results can be obtained by using a non-conservative approximation of the internal energy equation in the following form:

$$m_i \left(\varepsilon_i^{n+1} - \varepsilon_i^n\right) = -p_i^n\, \Delta V_i^{n+1}\,. \tag{12}$$

Here, the material pressure is multiplied by the overall change of the material volume. We have performed experiments similar to those presented in [3] and have found that the conservation of total energy is violated on the level of less than one percent. A detailed justification of our algorithmic choices, including the approximation (12) of the internal energy equation, is presented in Section 5.

Positivity of internal energy

The inequality required for the positivity of internal energy of the real material on the new time step can be written as

$$\Delta \mathcal{E}_i^{bulk} \geq p_i^n \sum_{k \in M(i)} \Psi_{i,k}\, \delta V_{i,k}^{max}\,, \tag{13}$$

where

$$\Delta\mathcal{E}_i^{bulk} = m_i\,\varepsilon_i^n - p_i^n\,\Delta V_i^{bulk}\,. \tag{14}$$

This is another linear inequality constraint with respect to limiters $\Psi_{i,k}$. The specific internal energy of void is always zero, therefore this constraint does not apply to a void sub-cell.

4.2.3. Controlling pressure equilibration

Another important property of closure models is the manner in which pressure equilibration is achieved in time[1]. Pressure equilibration should be achieved without oscillations and in such a way that the pressures of different materials approach equilibrium in a smooth fashion. The linear inequality constraints related to smooth pressure equilibration are essentially the same as for the case of the multimaterial cells with real materials [3]. The only difference is that the pressure of void is always zero.

Consider the evolution of the material pressure during a single time step. If the time step is small enough it can be assumed that the entropy is constant during the time step [2] and the following approximation for material pressure evolution may be used:

$$\tilde{p}_i^{n+1}(\Psi_{i,k}) = p_i^n - \rho_i^n\,(a_i^n)^2\Delta V_i^{n+1}\Big/\,V_i^n = \tilde{p}_i^{bulk,n+1} - \frac{\rho_i^n\,(a_i^n)^2}{V_i^n}\sum_{k\in M(i)}\Psi_{i,k}\,\delta V_{i,k}^{max}\,, \tag{15}$$

where the following pressures are given:

$$\tilde{p}_i^{bulk,n+1} = p_i^n - \frac{\rho_i^n\,(a_i^n)^2}{V_i^n}\,\Delta V_i^{bulk,n+1}.$$

The second term on the RHS of (15) is again a linear function of $\Psi_{i,k}$. For void, the pressure is zero by definition and therefore $\tilde{p}_i^{bulk,n+1} = 0$.

To achieve smooth equilibration, a temporarily targeted equilibrated pressure, $\bar{p}$, is computed from known quantities. The material pressures are intended to relax towards this target pressure in this particular time moment. In general, material pressures $p_i^{bulk,n+1}$ may be higher or lower than $\bar{p}$. However, the following inequality must always hold: $\max_i \tilde{p}_i^{bulk,n+1} \geq \bar{p} \geq \min_i \tilde{p}_i^{bulk,n+1}$. If a multimaterial cell does not contain void then we always choose

$$\bar{p} = \sum_i \alpha_i^n\,\tilde{p}_i^{bulk,n+1}. \tag{16}$$

If a multimaterial cell contains void then we have more options.

As the pressure in void is always zero and cannot change, Therefore, it is natural, to relax all material pressures towards zero. This means that in every cell containing void we set $\bar{p} = 0$. In Section 5.2 we will present a comparison of calculations which have been performed with $\bar{p} = 0$ and with $\bar{p}$ defined by the expression (16) in cells with voids - it turns out that these calculations are not sensitive to which of these options is used.

[1] Here we consider a situation in which no new forces are applied to the multimaterial cell after a certain transition time and contact is established.

[2] Strictly speaking the assumption of isentropy is admissible providing that the shock does not cross the multimaterial cell. Therefore, we can consider such an assumption as a simplifying approximation which leads to linearization of equation of state.

The limiters $\Psi_{i,k}$ are chosen in such a way that $\tilde{p}_i^{n+1}$ defined by equation (15) will, if possible, relax towards (or at least not diverge from) $\bar{p}$. The zero void pressure is fixed and as such is not affected by the limiters. A derivation similar to the one presented in [3] leads to another system of linear inequalities with respect to the limiters - which is summarized in the next Section.

4.2.4. Constrained optimization framework

For each multimaterial cell z, the following minimization problem is solved

$$\min_{\Psi_{i,k}} \left\{ \sum_i \left[\sum_{k \in M(i)} (1 - \Psi_{i,k})^2 \right] \right\} . \tag{17}$$

The linear constraints come from the volume bounds, positivity of internal energy and pressure equilibration conditions described in the previous sections. For each material i, the constraints for the limiters $\Psi_{i,k}$ are:

- The constraint related to the volume of a real material i:

$$\sum_{k \in M(i)} \Psi_{i,k}\, \delta V_{i,k}^{max} \geq (\kappa_{bot} - 1)\, V_i^{n+1,bulk} . \tag{18}$$

- For void, we have the following volume related constraint:

$$\sum_{k \in M(v)} \Psi_{v,k}\, \delta V_{v,k}^{max} \geq -V_v^{n+1,bulk} . \tag{19}$$

- The constraint related to positivity of real material internal energy (13):

$$m_i\, \varepsilon_i^n - p_i^n\, \Delta V_i^{n+1,bulk} \geq p_i^n \sum_{k \in M(i)} \Psi_{i,k}\, \Delta V_{i,k}^{max} . \tag{20}$$

- The constraints related to controlling pressure equilibration

$$\frac{V_i^n}{\rho_i^n\, (c_i^n)^2} (\tilde{p}_i^{bulk,n+1} - \bar{p}) \geq \sum_{k \in M(i)} \Psi_{i,k}\, \delta V_{i,k}^{max} \geq 0 , \quad \text{if } \tilde{p}_i^{bulk,n+1} \geq \bar{p} ; \tag{21}$$

$$\frac{V_i^n}{\rho_i^n\, (c_i^n)^2} (\tilde{p}_i^{bulk,n+1} - \bar{p}) \leq \sum_{k \in M(i)} \Psi_{i,k}\, \delta V_{i,k}^{max} \leq 0 , \quad \text{if } \tilde{p}_i^{bulk,n+1} \leq \bar{p} . \tag{22}$$

Remember that for multimaterial cell with void $\bar{p}$ is zero.

The constrained-optimization problem for finding the limiters $\Psi_{i,k}$ is evaluated as a quadratic optimization problem with linear inequality constraints [16]. In the current implementation, the "QL" software [21] is used to solve this problem.

4.2.5. Void closure detection

After we solve the constrained optimization problem and limiter values are determined we need to update all material quantities. In particular, the updated volume of void sub-cells is computed. If it is "zero" then it means that the void has *closed*. Therefore, we need to update the status of the multimaterial cell as it now does not contain void and the corresponding sub-cell must be removed.

More details can be found in [5]. In particular, in [5] we present explicit solution of the constrained optimization problem in the case when multimaterial cell contains one real material and void.

5. Algorithmic choices

5.1. Kinetic energy fix in arbitrary Lagrangian-Eulerian methods

An important aspect of ALE methods is the techniques used for remapping variables from the Lagrangian to the rezoned mesh. In this paper we use Eulerian=Lagrange+Remap version of ALE, such that after Lagrangian step data is transferred back to the initial Eulerian mesh.

The remap has to *conserve* the same quantities and in the same form as Lagrangian step does - conservation of mass, momentum and total energy - to ensure the conservation of the overall ALE method.

If the total energy after remap is computed as the sum of the conservatively remapped internal energy and the kinetic energy computed from the remapped velocity, which is computed from conservatively remapped momentum and remapped mass, then it will not be conservative, because some dissipation is introduced during the velocity remap.

Some codes ignore this discrepancy. Other codes (see, for example, [9, 6, 19, 20, 8, 4]) use an approach often termed the *kinetic energy fix* to restore total energy conservation completely or locally near shock front. The kinetic energy fix is critical for correct computing flows with shock waves. In this approach one also conservatively remaps the kinetic energy. The full discrepancy (or part of it) between actual kinetic energy computed from remapped velocity and remapped kinetic energy is added to the internal energy, such that the total energy is conserved exactly (or total energy imbalance is decreased).

To demonstrate the importance of conservation of total energy we consider the computation of a Sedov-like shock. The initial conditions are $\rho = 1$, $u = 0$ everywhere. The internal energy is initialized as $\varepsilon = 100$ in the source region from 0 to 0.01 and $\varepsilon = 0.0001$ in the rest of the real material. This is not a standard Sedov problem with point source but rather a *finite size* source Sedov-like problem. In our experiments we choose a number of cells such that one of the nodes always lies at $x = 0.01$. This means that for refined meshes there are more cells in the region with high internal energy but the initial total energy in the high energy part of the domain is always the same and equal to $0.01 \times 100 = 1$. The computational domain is the segment $[0 : 1]$ and both boundaries are solid walls. The final time is $t = 0.5$. In Fig.2 we present four graphs - the reference solution obtained on a very fine grid, and the results of three calculations with different treatments of the kinetic energy discrepancy on a mesh of 2500 cells.

The first treatment is the full kinetic energy fix - this is a completely conservative method - there is no loss of total energy. Such an approach produces numerical results which are very close to the reference solution. The second approach is no kinetic energy fix at all. In this approach we lose approximately 28% of the total energy and the results are absolutely wrong. The final approach is to perform the kinetic energy fix only for cells in which the ratio of the artificial viscosity to the pressure is greater than 1%. In this case we lose approximately 1.3% of the total energy and

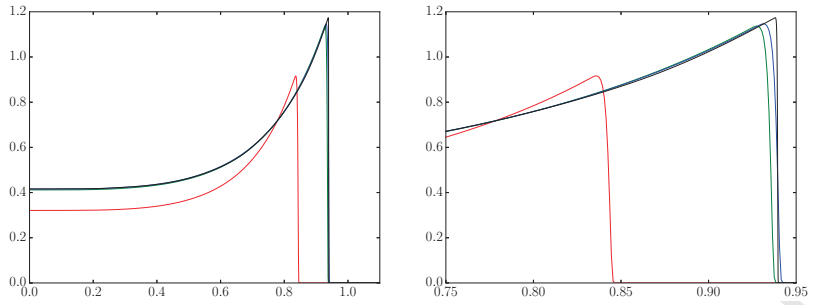

(a) Pressure (b) Pressure – zoom in

Fig. 2: Pressure in the Sedov-like problem demonstrating the importance of the kinetic energy fix. Comparing exact solution (–), no KE fix (–), KE fix with switch (–), full KE fix (–).

the results are still very accurate. Therefore, when modeling flows with shocks we have to use some form of kinetic energy fix. As will be shown in the next Section the use of the artificial visocity/pressure switch for the kinetic energy fix is critical for smooth flows.

5.2. Algorithmic choices in closure model

To apply the closure model described in Section 4 we have to make several algorithmic choices. We set κ_{bot} in inequality (7) equal to 0.1.

In Fig. 3 we present the results for the different algorithmic choices for the expansion in to vacuum problem. This problem is also termed the Riemann problem in the presence of a vacuum [22]. We consider the case where an ideal gas on the left of the origin is initially at rest. The gas has a ratio of constant volume specific heat capacity to constant pressure specific heat capacity ($\gamma = 1.4$), a constant density $\rho_L = 1$ and constant pressure $p_L = 0.4$. The vacuum is on the right of the origin.

If we denote the adiabatic speed of sound of the initial state by a_L, where $a_L = \sqrt{\gamma(\gamma-1)\varepsilon_L}$, then the solution, $\mathbf{W}(x,t) = (\rho,\ u,\ p)$ is

$$\mathbf{W}(x,t) = \begin{cases} \mathbf{W}_L & \text{if} \quad \frac{x}{t} \le -a_L \\ \mathbf{W}_{Lfan} & \text{if} \quad -a_l < \frac{x}{t} < \frac{2\,a_L}{\gamma-1} \\ \mathbf{W}_0 & \text{if} \quad \frac{x}{t} \ge \frac{2\,a_L}{\gamma-1} \end{cases}, \tag{23}$$

where

$$\mathbf{W}_{Lfan}(x,t) = \begin{cases} \rho = \rho_L \left[\frac{2}{\gamma+1} - \frac{\gamma-1}{(\gamma+1)\,a_L}\,\frac{x}{t}\right]^{\frac{2}{\gamma-1}} \\ u = \frac{2}{\gamma+1}\left[a_L + \frac{x}{t}\right] \\ p = p_L \left[\frac{2}{\gamma+1} - \frac{\gamma-1}{(\gamma+1)\,a_L}\,\frac{x}{t}\right]^{\frac{2\gamma}{\gamma-1}} \end{cases}. \tag{24}$$

The boundary between the gas and vacuum is moving with the velocity

$$u_{free} = \frac{2}{\gamma-1}\,a_L = \frac{2\,\sqrt{\gamma(\gamma-1)\,\varepsilon}}{\gamma-1} = 3.741657\,.$$

The exact solution of this problem conserves total energy.

In our numerical calculations we use the domain $[0:2.5]$ and the real gas is contained within the subregion $[0:1]$ and the rest of the domain is occupied by the vacuum (void in the calculations). The extensive numerical results

for problem are presented in Section 6.1.2, in this section we just present some results which justify our algorithmic choices for the void closure model.

In Fig. 3a we show graphs for the specific internal energy at $t = 0.5$ with 10000 cells for different algorithmic choices. For all the calculations $\bar{p} = 0$. In the figure caption "switch off" means that we are performing the full kinetic energy fix and "switch on" meant that we use the switch based on the ratio of the artificial viscosity and pressure. The $p^* = 0$ means that we use internal energy update in the conservative form (11) with $p^* = 0$; the $p^* = p_{mat}$ means that we use internal energy update in the non-conservative form (12). The first conclusion from these results is that we

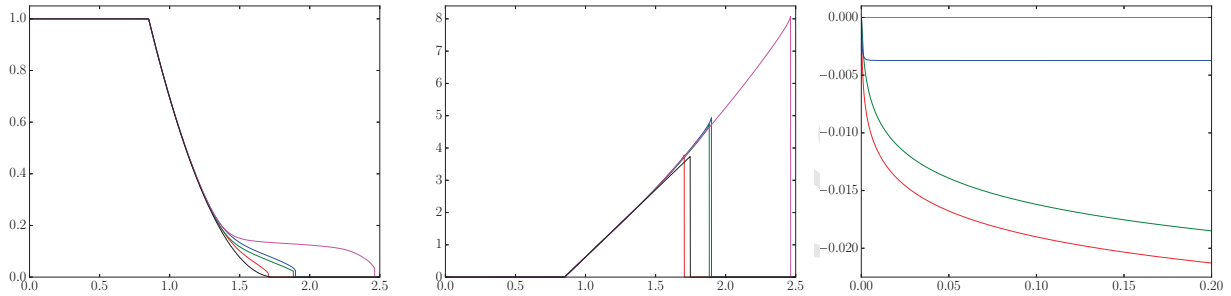

(a) Specific internal energy

(b) Velocity

(c) Time history of the relative total energy imbalance (final − initial) [%]

Fig. 3: Expansion into vacuum problem, different algorithmic choices: switch on, $p^* = p_{mat}$ (–), switch on, $p^* = 0$ (–), switch off, $p^* = p_{mat}$ (–), switch off, $p^* = 0$ (–), exact solution (–).

have to use the switch, because completely conservative calculations ("switch of" and $p^* = 0$) give very inaccurate results. The velocity graphs presented in Fig. 3b confirm this conclusion.

From these figures we can also conclude that the best results are achieved when we use $p^* = p_{mat}$. Clearly, using the switch option for kinetic energy fix and $p^* = p_{mat}$ makes our method not completely conservative. The influence of these choices on conservation is demonstrated in Fig. 3c - the maximum loss of the total energy is less than 0.025%.

Finally we will demonstrate that our model is not sensitive to the choice of $\bar{p}$. In Fig. 4 we present results for "switch on", $p^* = p_{mat}$ and two options for $\bar{p} = 0$ and $\bar{p}$ computed as volume fraction average, (16). To see the difference between these options we need to zoom in on the solution. In the calculations with $\bar{p} = 0$ the front of free boundary moves faster.

To summarize our algorithmic choices for closure model we use the kinetic energy fix with the artificial viscosity/pressure switch which is on when this ratio is greater than 1%; we use the non-conservative internal energy update - (12); and we use $\bar{p} = 0$.

Let us note, that we do not claim that our algorithmic choices are optimal. This is why this paper has the word "framework" in its title. The optimal choice of the parameters may be problem dependent and will require more investigation.

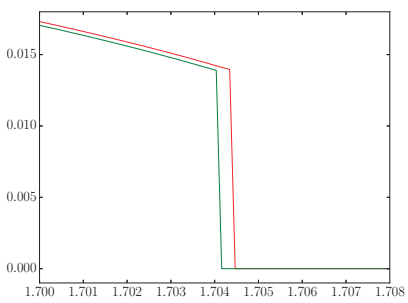

(a) Specific internal energy – zoom in

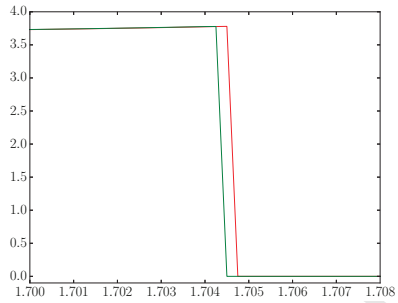

(b) Velocity – zoom in

Fig. 4: Comparison of options for $\bar{p}$ for expansion in to vacuum problem. Comparing $\bar{p}$ computed as volume fraction average (–), $\bar{p} = 0$ (–).

6. Numerical examples

Three one-dimensional test problems are presented in Section 6.1. The first problem is a *sanity check* problem which involves the movement and collision of cold blocks of gas – Section 6.1.1. It demonstrates that our void closure treatment is working and gives overall plausible results. In Section 6.1.2 we present results for the expansion of an ideal gas into vacuum and the subsequent collision of the free boundary with a wall. The expansion into vacuum (until the free boundary hits the wall) has an analytical solution. It is observed that the position of the free boundary is not accurate, however, after the free boundary hits the wall the solution converges to a reference solution. In the last one-dimensional example, Section 6.1.3, we explore how a Sedov-like shock wave interacts with the free boundary. The conclusions are the same as for the expansion in to vacuum problem.

The two-dimensional tests are presented in Section 6.2. In Section 6.2.1 we present a diagonal projectile-plate impact. Here we demonstrate the robustness of our method and give some comparisons with using an artificial "light" gas environment instead of void. This numerical example confirms our speculations in the Introduction about the problems arising with the usage of an artificial gas. In the following Section 6.2.2 we present an example of a shock wave interacting with a spherical void cavity. It gives plausible and the expected results – the void completely closes and the shock front is accelerated in the location of the void cavity. In Section 6.2.3 we present the results for a simplified model of a shaped-charge-like problem. It is intentionally set up so that it shows some of the features seen in real shaped charge simulations, but uses a simplified geometry and does not include more complex material features (only ideal gas EOS). That way the interested reader can attempt to reproduce our results or compare her/his own method for void closure. Finally, in Section 6.2.4 we present a sneak peek of the application of of our new method for solving a realistic shaped charge problem with appropriate models for high-explosives and solids. This test is the unconfined shaped charge from [23, 2].

6.1. One-dimensional tests

6.1.1. Movement and collision of cold blocks of gas

In this Section we present a *sanity check* example. The statement of the problem is as follows:

The computational domain is the segment $[-2, 2]$, the left and right boundaries are walls. There are two blocks of cold ideal gas, both with the following properties: $\gamma = 5/3$, $\rho = 1$, $\varepsilon = 1.0 \cdot 10^{-9}$. The first, longer, block, initially

occupies the segment $[-1.75, -0.5]$ and its velocity is 1. The second, shorter, block occupies the segment $[0.5, 1.5]$ and its velocity is -1. The rest of the computational domain is filled with void cells - see Fig.5.

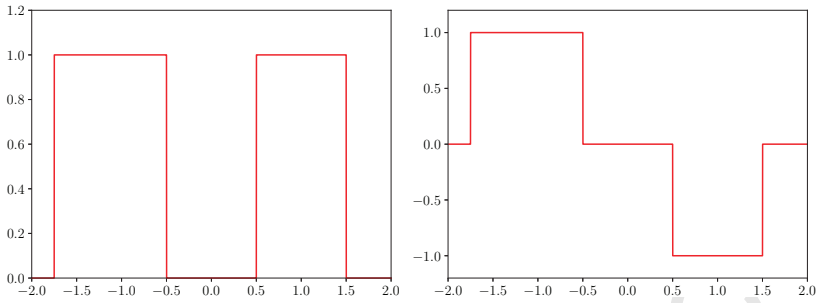

(a) Density (b) Velocity

Fig. 5: Cold blocks collision problem – the initial conditions for density and velocity.

We perform the calculations using our new treatment of void closure using 10000 cells. In Fig. 6 we present the density and velocity at $t = 0.25$. It demonstrates that our new void treatment allows us to reproduce translation of solid bodies exactly.

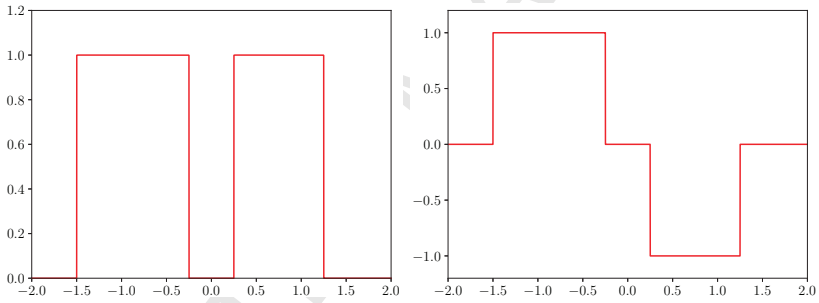

(a) Density (b) Velocity

Fig. 6: Cold blocks collision problem, $t = 0.25$ – intermediate stage.

In Fig. 7 we present the density, velocity and pressure at $t = 0.501$, that is, right after the collision. All void cells between the blocks are closed and the density and the pressure start to grow near the collision point.

After the collision, two shocks form traveling in opposite directions within each block. In Fig. 8 we present the density, velocity, specific internal energy and pressure plots for the time moment $t = 1.2$ when the shock front in the right block has almost reached its right boundary. The standard wall heating phenomenon can be observed, which manifests itself as a dip in the density and an overshoot in the specific internal energy, while the velocity and pressure are flat.

After the shocks have reached the free boundaries of both blocks, the expansion in to vacuum starts. This moment, $t = 1.5$, is shown in Fig. 9. The expansion has obviously started earlier for the shorter right hand block.

In Fig. 10 time moment $t = 2.0$ is shown where the expansion wave from the right block has reached the right wall and all the voids are closed on the right side.

Finally, in Fig. 11, we show the time moment $t = 2.5$ where all the void is closed, and shock waves are starting to

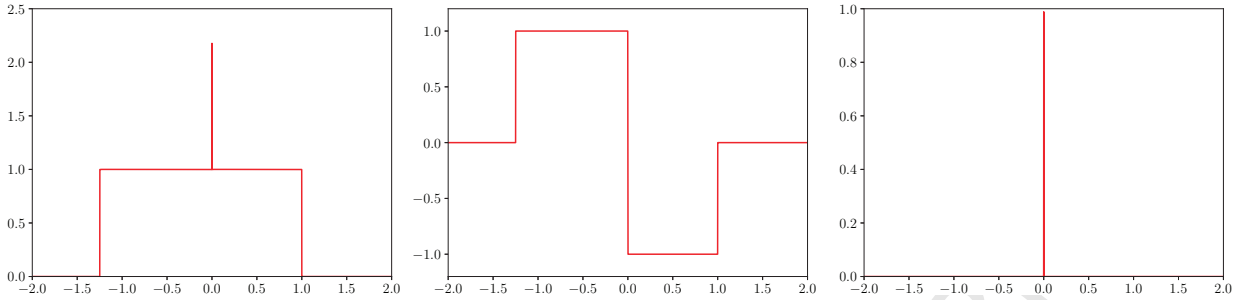

(a) Density (b) Velocity (c) Pressure

Fig. 7: Cold blocks collision problem, $t = 0.501$ – just after collision.

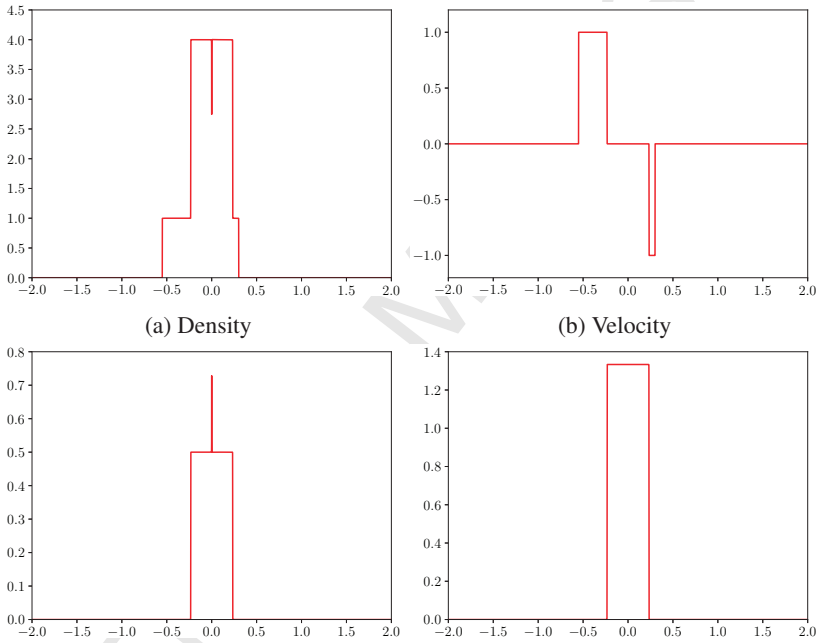

(a) Density (b) Velocity

(c) Specific internal energy (d) Pressure

Fig. 8: Cold blocks collision problem, $t = 1.2$ – the shock has almost reached the right boundary of the right block.

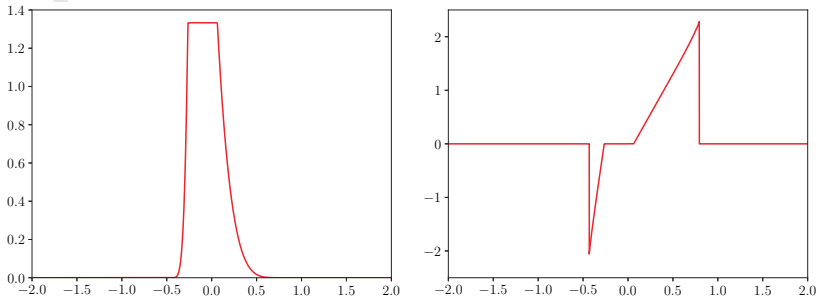

(a) Pressure (b) Velocity

Fig. 9: Cold blocks collision problem, $t = 1.5$ – expansion into vacuum is starting.

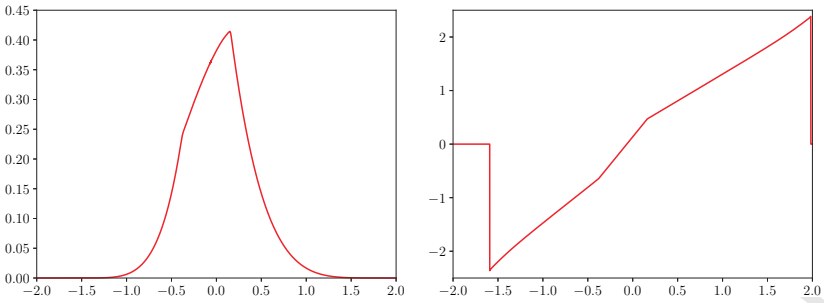

(a) Pressure (b) Velocity

Fig. 10: Cold blocks collision problem, $t = 2.0$ – the right end of the right block has reached the right wall.

form from the reflections at both the left and right walls.

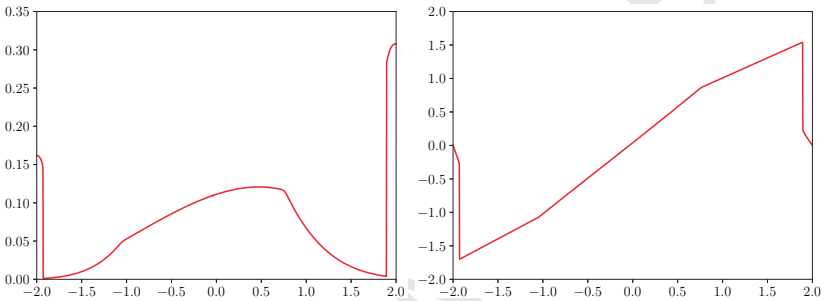

(a) Pressure (b) Velocity

Fig. 11: Cold blocks collision problem, $t = 2.5$ – the void is completely closed in the entire domain and the reflection at both walls is visible.

6.1.2. Expansion into vacuum

The second problem is the expansion of ideal gas into vacuum, which was fully defined in Section 5.2.

First we perform a Lagrangian simulation with only pure cells by explicitly imposing free boundary conditions at the right boundary.

The results for velocities and pressures at different mesh resolutions are compared with the exact solution at $t = 0.25$ in Fig.12. It is clear from Fig.12 that the convergence (if any) of the Lagrangian calculations is very slow and

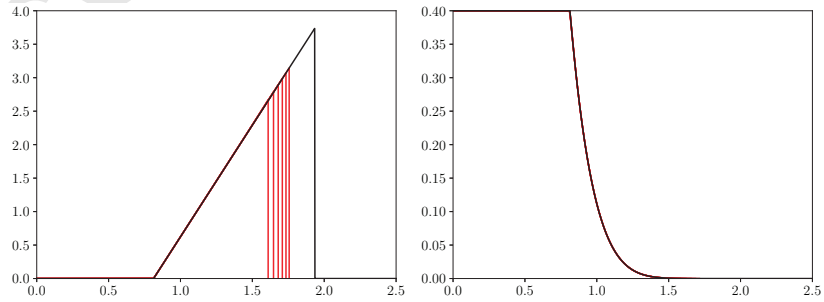

(a) Velocity (b) Pressure

Fig. 12: Expansion in vacuum – exact solution (–) and the Lagrangian calculation with free boundary (–) using 1000, 2000, 4000, 8000, 16000, 32000 cells (higher resolutions produce a faster boundary), $t = 0.25$.

the position of the free boundary is very inaccurate even for such high resolutions as 32000 cells. This is a very well known result which is usually attributed to the presence of a very big cell next to the free boundary (the interested reader can refer to a recent presentation [17]).

However, to understand the accuracy issues one also needs to look not just at the position of the free boundary but also at the values of the density, specific internal energy and pressure near the free boundary. In Fig.13 we show a zoom in of the density, specific internal energy and pressure profiles near free boundary for two spatial resolutions as well as the profile of the exact solution. As one can see from Fig.13, the values of the Lagrangian numerical solution

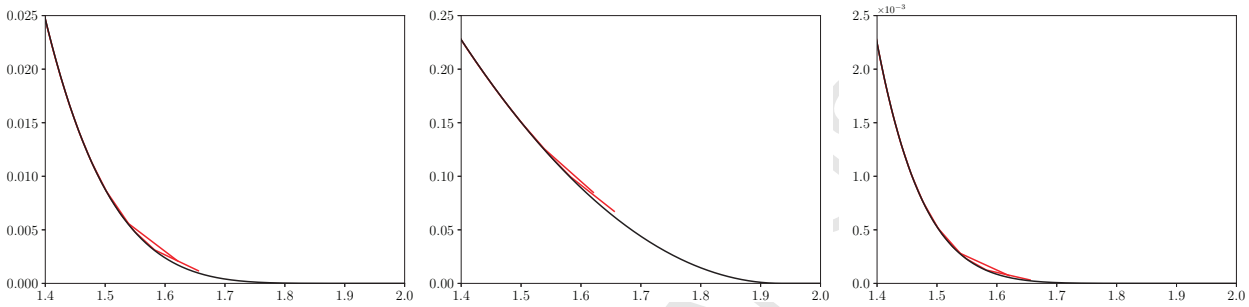

(a) Density (b) Specific internal energy (c) Pressure

Fig. 13: Zoom of the density, specific internal energy and pressure profiles near the free boundary. Two spatial resolutions – the Lagrangian calculation using 4000 and 8000 cells (–) and the exact solution (–).

are slightly larger compared to the exact solution. However, in general the values of the pressure are small near the free boundary. The real question is what will happen after the free boundary interacts with some obstacle. Clearly, the start of the interaction will be delayed in comparison with exact solution, but it is not clear how it will affect the resulting flow afterwards – pressure in the exact solution near the free boundary goes to zero. We will address this question later in this section.

Now, we will use our new void closure method as described in the previous sections to solve the same problem. Let us remember that we are using an Eulerian=Lagrange+Remap approach. Therefore we need to use a longer computational domain because the interface between real gas and vacuum will move throughout the domain. In our calculation the computational domain is $[0, 2.5]$. The gas initially occupies the segment $[0, 1]$ as in the Lagrangian calculations with free boundary. The rest of the domain, $[1, 2.5]$, is initially filled with void. In Fig.14 we show the velocity and pressure obtained by our new method at $t = 0.25$ for different spatial resolutions so that these pictures can be compared with pictures in Fig. 12. The number of cells is chosen so that the number of cells initially containing the real gas is the same as in the pure Lagrangian calculation. The total number of cells is then 2.5 times larger than in the Lagrangian calculations.

The position of the interface between gas and void, which corresponds to the position of the free boundary in pure Lagrangian calculations, apparently moves much faster compared to the Lagrangian calculations. It also appears that it does not converge to the exact solution and the interface is moving faster and faster each time the spatial resolution increases.

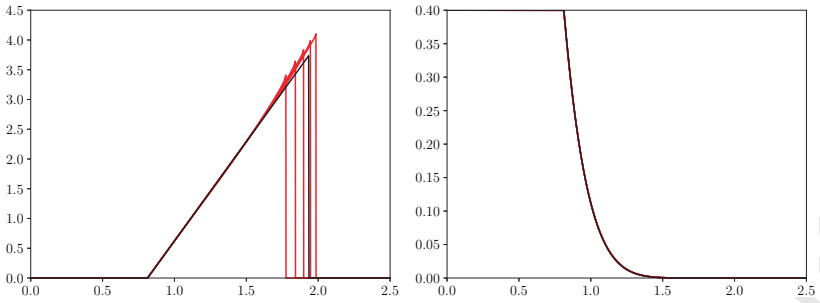

(a) Velocity (b) Pressure

Fig. 14: Expansion in vacuum – exact solution (–) and Eulerian=Lagrange+Remap calculations with the void closure treatment (–) using 2500, 5000, 10000, 20000, 40000 cells (higher resolutions produce faster boundary), $t = 0.25$.

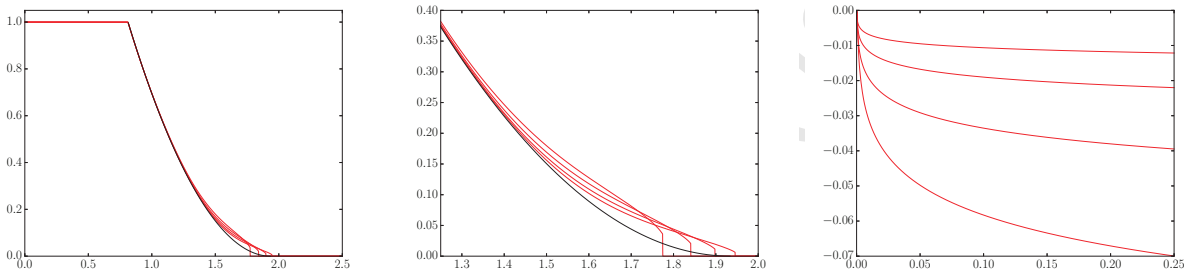

(a) Specific internal energy (b) Specific internal energy – zoom in (c) Time history of the relative total energy imbalance (final − initial) [%]

Fig. 15: Expansion in vacuum – convergence demonstration. Exact solution (–) and Eulerian=Lagrange+Remap calculations with the void closure treatment (–) using 2500, 5000, 10000, 20000 cells (higher resolutions produce faster boundary and lower total energy imbalance), $t = 0.25$.

Let us now analyze convergence for specific internal energy, density, pressure. Because our method is not exactly conservative it is also important to show how the imbalance in total energy changes with increase in resolution. The most sensitive quantity is specific internal energy. We show graphs of specific internal energy at the final time, $t = 0.25$, for different mesh resolutions in the left and middle panels in Fig. 15. In the right panel of this figure we show the total energy discrepancy as function of time for the different mesh resolutions. We have also made a quantitative analysis. In Table 1 we present discrete $L1$ norms for errors in density, specific internal energy and pressure and the imbalance of total energy at the final time $t = 0.25$. In the last row of this table we give estimates for the convergence rate based on results for two finest meshes. As expected the worse convergence rate is for specific

Number of cells	Density	Inter. Ener.	Pres.	Disb. Tot. En.
2500	1.47E-3	1.66E-2	5.81E-4	6.99E-2
5000	8.62E-4	1.33E-2	3.28E-4	3.94E-2
10000	4.91E-4	1.09E-2	1.81E-4	2.20E-2
20000	2.81E-4	8.92E-3	1.001E-4	1.21E-2
Conv. rate	0.81	0.29	0.85	0.86

Table 1: Expansion in to vacuum - convergence rates. Discrete $L1$ norms for errors in density, specific internal energy and pressure and imbalance of total energy at final time $t = 0.25$. Last row - estimated convergence rate based on two finest meshes.

internal energy, for other quantities it is close to first order.

We give more details relating to this problem below. In Fig.16 we present a zoom of the density, specific internal energy and pressure near the position of the interface. The values of all the parameters in the void are zero. The

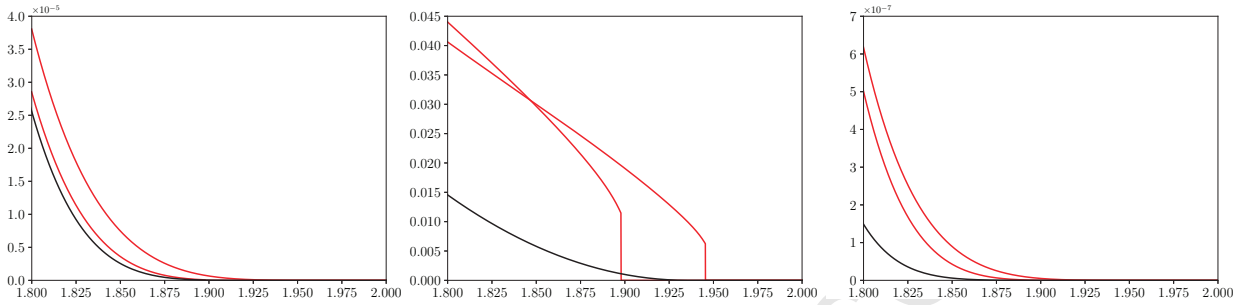

(a) Density (b) Specific internal energy (c) Pressure

Fig. 16: Expansion in vacuum – exact solution (–) and Eulerian=Lagrange+Remap calculations with the void closure treatment (–) using 10000 and 20000 cells (higher resolution produces results closer to the exact solution and a faster boundary), $t = 0.25$. Zoom for density, specific internal energy and pressure.

conclusion from Fig.16 is similar to the one from Fig.13. That is, clearly the numerical values are not very accurate, especially the values for the specific internal energy. However, the pressure values are very low and it is not clear how it will affect the flow if the interface collides with some obstacle.

To answer this question we have performed the following experiment. The exact solution at the time $t = 0.4009$ was computed. This is the time when the free boundary reaches the wall at $x = 2.5$ and is shown in Fig.17.

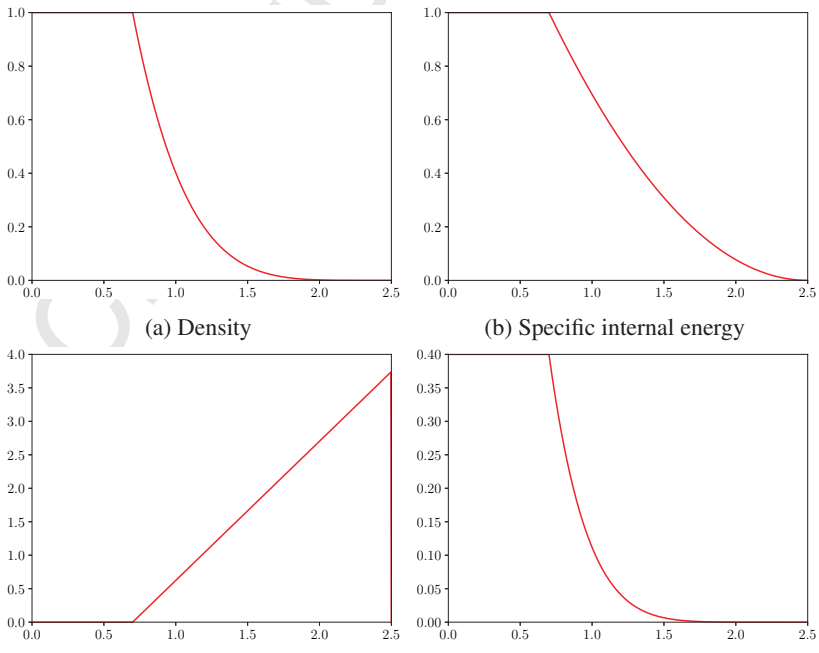

(a) Density (b) Specific internal energy

(c) Velocity (d) Pressure

Fig. 17: Exact solution for expansion in vacuum at $t = 0.4009$, when the free boundary reaches the right boundary of the domain (wall).

We use this exact solution as the initial data for our Eulerian=Lagrange+Remap calculations to create a reference solution at $t = 0.8$, which corresponds to the solution at $t = 1.2009 = 0.4009 + 0.8$ starting with the position of the interface at $x = 1$. The reference solution is computed using 80000 cells. Then we compute our numerical solution in which the free boundary initially at $x = 1$ and run it till $t = 1.2009$. At this moment all voids are closed, the wave is reflected from the wall and we can compare this solution with our reference solution. This comparison is shown for various resolutions in Fig.18. We only show the pressure profiles here.

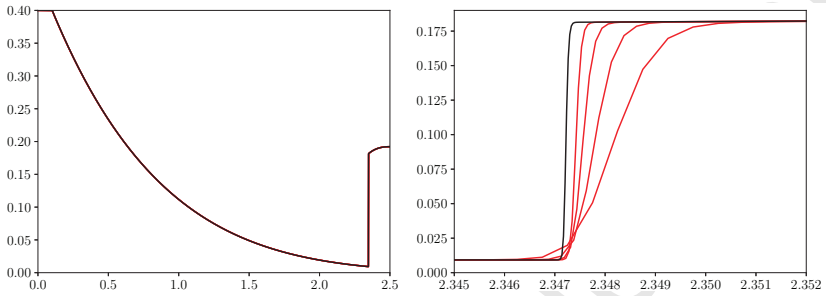

(a) Pressure profile (b) Zoom at shock

Fig. 18: Convergence after the reflection from the wall. Reference solution (–) and Eulerian=Lagrange+Remap calculations with the void closure treatment (–) using 5000, 10000, 20000, 40000 cells (higher resolutions are closer to the reference solution), $t = 1.2009$.

One can only see the differences in the zoomed in picture on the right panel in Fig. 18. One can clearly see that the numerical solutions obtained using void closure treatment do converge to the reference solution and the convergence is visually close to first order.

6.1.3. Sedov-like release in to vacuum

In this section we consider the interaction of a Sedov-like shock as described in Section 5.1, with a free boundary and the reflection of the rarefaction wave that is formed with the wall. The geometry of the mesh and the boundary conditions are the same as for the expansion in to vacuum problem. The initial condition are the same as described in Section 5.1.

The initial conditions produce a Sedov-like wave which is shown in Fig.19 for $t = 0.5$. A small velocity can be seen in the gas near the interface between the gas and the void, which is due to the initially small but non-zero specific internal energy in the gas (which creates a non-zero pressure gradient at the interface).

After the wave reaches the first cell containing void (the free boundary), the rarefaction wave moves to the left while reducing the peak of the Sedov-wave and the free boundary moves to the right, as seen in Fig. 20. We are not aware of an analytical solution for this problem.

First we run until $t = 0.75$, when the Sedov-like wave has reached the free boundary and a rarefaction wave has started to move to the left (and the free boundary has started moving to the right). In Fig. 20 and Fig. 21 we present the results using our new void closure treatment for different mesh resolutions. The results are similar to those presented in the previous section for the expansion into vacuum – there is again no convergence in the position of the free boundary, but the pressure profiles are very close and the pressure near the free boundary is very small.

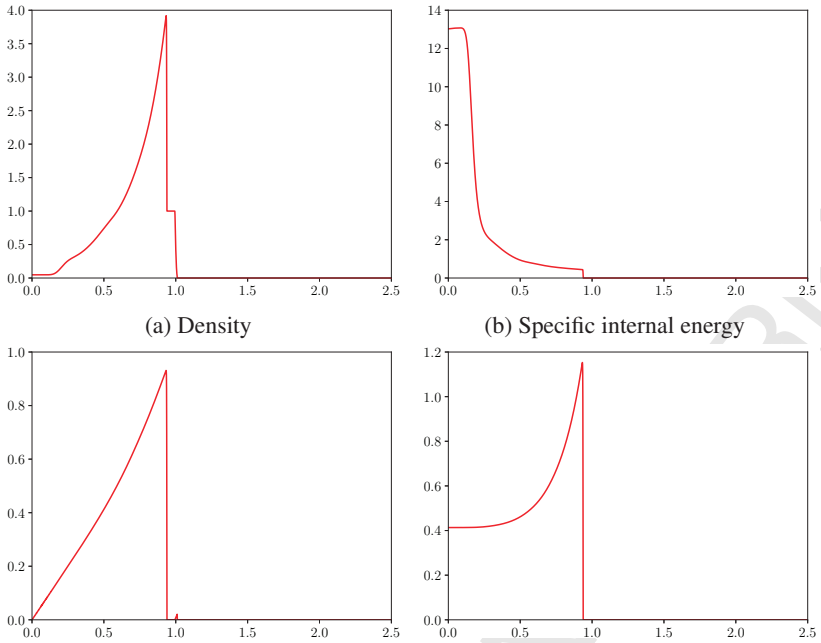

(a) Density (b) Specific internal energy

(c) Velocity (d) Pressure

Fig. 19: Sedov-like wave formed by the finite size source before it reaches the free boundary.

.

In Fig. 22 we present the profile of pressure at the moment $t \approx 0.862$ for 10000 cells, when all the void sub-cells have closed and the wave is about to start to reflect from the wall. This can be compared with Fig. 17.

In Fig. 23 we demonstrate the convergence for the Sedov-like problem after the reflection from the wall at time $t = 2.00$, we present only pressure profiles.

One can clearly see that the numerical solution obtained by using the void closure treatment converges to the reference solution.

6.2. Two-dimensional tests

6.2.1. Diagonal projectile-plate impact

In this section we present a simplified projectile-plate impact problem in the $(x, y) \in [0 : 2] \times [0 : 2]$ computational domain. An 80×80 computational mesh is used for most of the simulations of this problem. Both the projectile and the plate are modeled as ideal gases with different properties:

- **Projectile** – $\gamma = 50,\ \rho = 20,\ p = 1 \cdot 10^{-7}, \mathbf{u} = (0.2, 0.05)$, initially occupies the region:

$$(x, y) \in ((0.225, 0.7), (0.725, 0.825), (0.675, 1.025), (0.175, 0.9))$$

- **Plate** – $\gamma = \frac{5}{3},\ \rho = 15,\ p = 1 \cdot 10^{-7}, \mathbf{u} = (0, 0)$, initially in the region

$$(x, y) \in (1, 0) \times (1.1, 2)$$

The rest of the domain is filled with void or artificial gas – the initial geometry is shown in Fig.24.

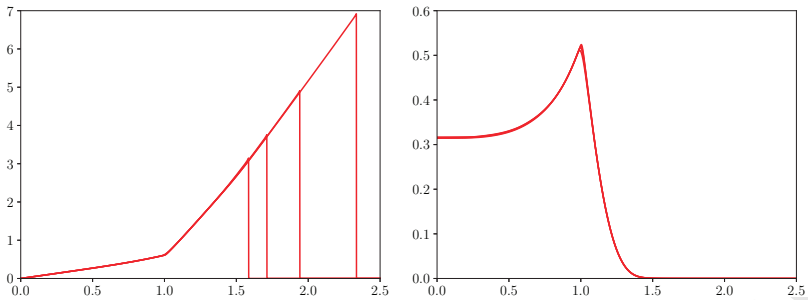

(a) Velocity (b) Pressure

Fig. 20: Sedov-like problem – Eulerian=Lagrange+Remap calculations with void closure treatment, 2500, 5000, 10000, 20000 cells (higher resolutions create faster interfaces), $t = 0.75$.

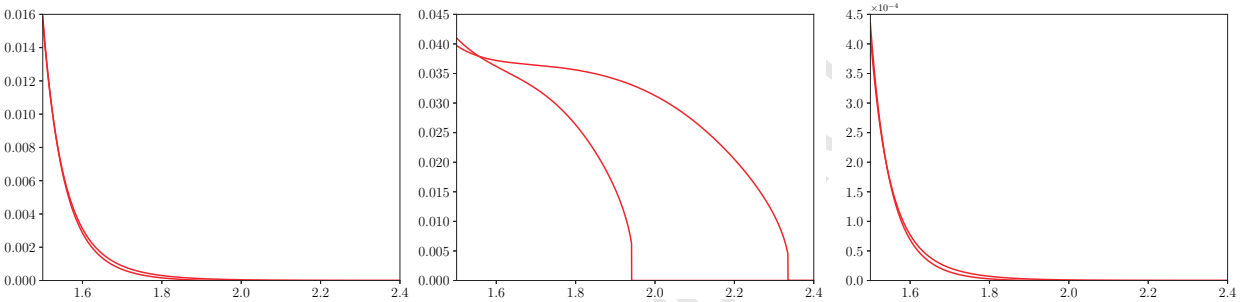

(a) Density (b) Specific internal energy (c) Pressure

Fig. 21: Sedov-like problem – zoom of the Eulerian=Lagrange+Remap calculations with void closure treatment, 10000 and 20000 cells (higher resolutions create faster interfaces with slightly higher densities and pressures in the neighboring real gas), $t = 0.75$.

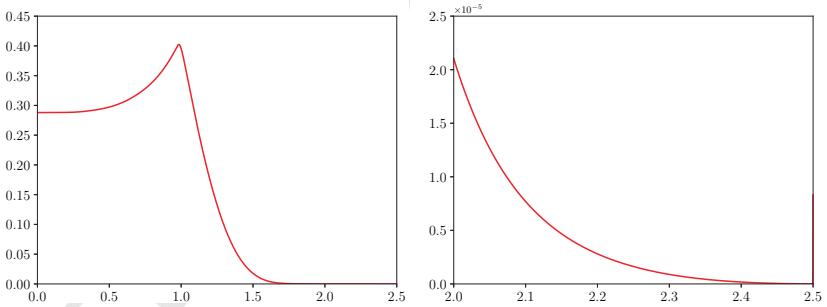

(a) Pressure profile (b) Zoom at pressure near the wall

Fig. 22: Sedov-like problem - calculation with 10000 cells, at $t \approx 0.862$. All the void cells have just closed.

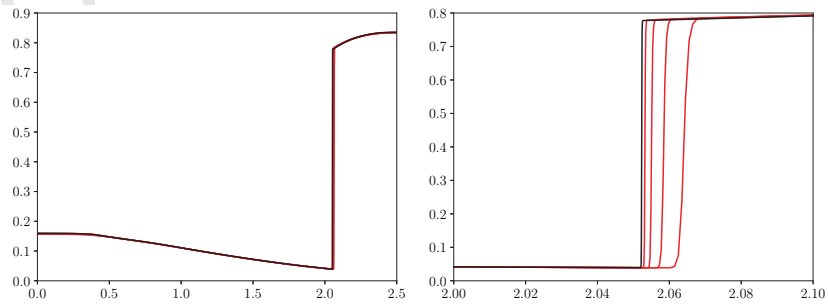

(a) Pressure profile (b) Zoom at shock

Fig. 23: Convergence after reflection from the wall, $t = 2.00$. Reference solution obtained by calculation on 40000*cells* (–) and solutions obtained by using the void closure treatment (–) using 2500, 5000, 10000, 20000 cells. Higher resolutions are closer to the reference.

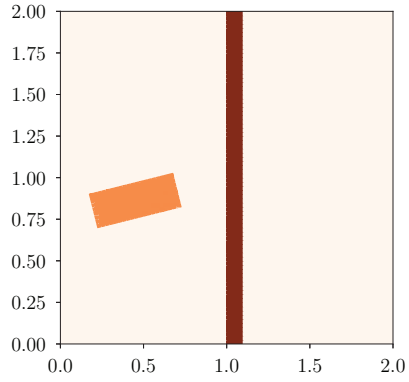

Fig. 24: Initial geometry of the projectile-plate impact test.
■ "projectile",
■ "plate',
■ void or artificial "light gas".

Using this example we will demonstrate the problems of using artificial gas to model void and show the robustness of our new closure model for voids. Let us note that for the artificial gas we use the IA-SSD closure model for multimaterial cells described in [3] with the modification for the treatment of the internal energy equation at the sub-scale stage as described in Section 4.2.2.

In this problem we can distinguish two phases. In the first phase (approx. $t \in [0, 1]$), the projectile moves freely through the void (or artificial gas). In the second phase the projectile interacts with the plate. We compare the performance of our method with a simulation using an artificial gas as a replacement for the void in both phases.

We will start by presenting the results obtained with our new method for the treatment of voids in multimaterial cells. In Fig. 25 we present results for different time moments. The left column shows the material and the interface reconstruction plots. We also present density plots in the middle column and velocity plots in the right column. At $t = 3$ the void between both materials is completely closed and no cavities remain. At $t = 4.5$, fragmentation of the projectile material begins and an instability is seen on the boundary. Then, at $t = 6$ the results are shown before the plate hits the boundary.

We now compare the results of computations using the new void treatment with three different types of artificial gas. Since we do not know what parameters to use for the artificial gas. Ideally, the artificial gas should not affect the shapes of the real materials and the simulations should be robust. We use the following initial parameters for the artificial gases:

1. $\gamma = \frac{5}{3}$, $\rho = 10^{-3}$ – high gamma/high density,
2. $\gamma = \frac{5}{3}$, $\rho = 10^{-7}$ – high gamma/low density,
3. $\gamma = 1.001$, $\rho = 10^{-7}$ – low gamma/low density.

The first type of gas has air-like properties, while the other two are artificial materials. In all cases the initial pressure is 10^{-7} both in the projectile and the plate (and in the artificial gas as well). From a theoretical point of view one may prefer artificial gas #3 – low gamma/low density – because it is very light and compressible, however, we will see that using such an artificial gas can cause robustness problems for the code.

At $t = 1$, the velocity distribution is shown in Figure 26 for different artificial gases and void. Lower 40×40 resolution simulations are presented in this Figure to improve the readability of the velocity vector plots. We can see how the artificial gas is affected by the motion of the projectile (the shape of the projectile itself is not visibly altered). We would like to mention again that one needs to solve the full system of hydrodynamics equations for the artificial gas representing void, which can be quite expensive. In addition to the expense it also causes a time step drop in the artificial gas materials with very low densities – see Fig. 27 for the time step behavior of the different artificial gases and the void treatment. One can also observe that the time step for the high gamma/high density artificial gas is even

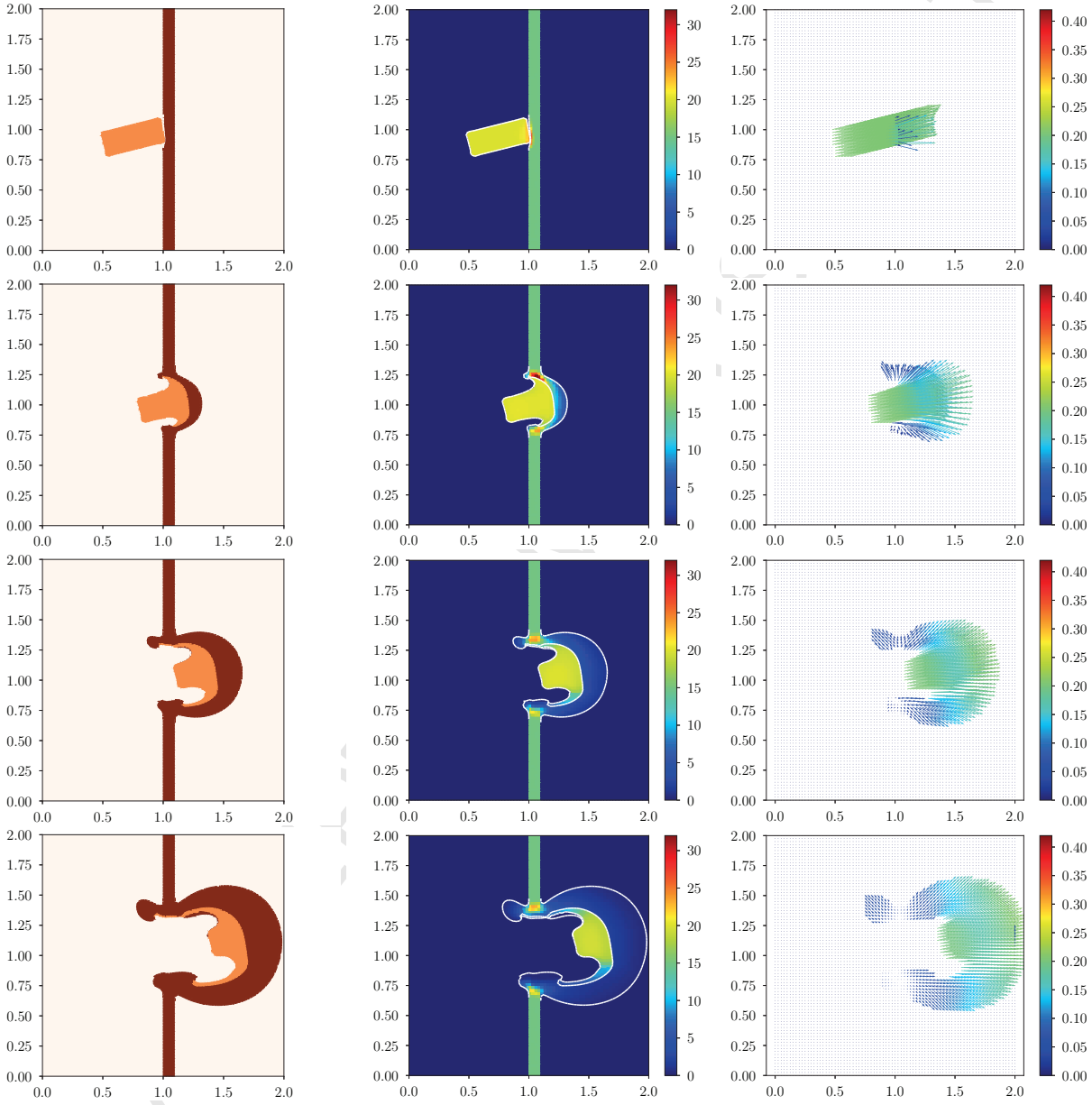

(a) Mat. distribution (b) Density (c) Velocity

Fig. 25: Diagonal projectile-plate impact, new void treatment, 80×80 mesh, $t = 1.5, 3, 4.5, 6$ from top to bottom.

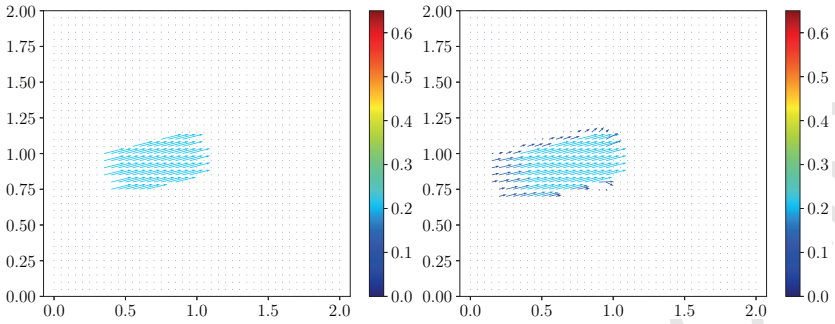

(a) Void
$n_{step} = 21$

(b) High gamma/high density artificial gas
$n_{step} = 17$

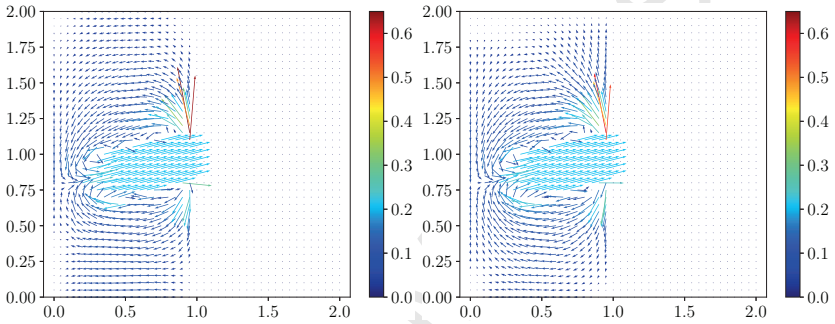

(c) High gamma/low density artificial gas
$n_{step} = 110$

(d) Low gamma/low density artificial gas
$n_{step} = 85$

Fig. 26: Diagonal projectile-plate impact – comparison of the velocity distribution at $t = 1$ (before impact) for void and various light gas environments, 40×40 mesh.

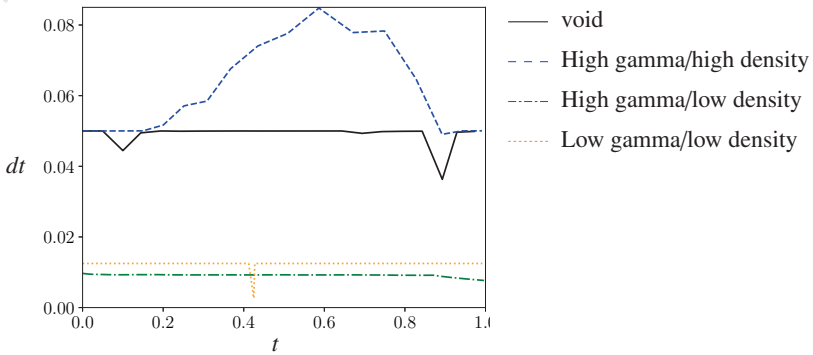

Fig. 27: Diagonal projectile-plate impact – time step comparison for void and light gas computations during the initial flight phase, 40×40 mesh.

larger than in the void case. However, in this case the shapes of the real materials are visibly altered after the impact (see Fig. 28).

At $t = 3$, the artificial gas that remains between the projectile and the target is clearly visible in the left panel in Fig. 29.

At later time moments we can see that when using artificial gas the shape of the deformed projectile is slightly different than in the void case. Also the expanding plate material is propagating more slowly due to the resistance of the artificial gas. In the velocity plot, we can see that the void calculation gives a smoother velocity profile with less artifacts.

For the other two types of artificial gas the time step degenerates after the impact and the simulation fails.

The conclusion for this is that although an artificial light gas computation with reasonable accuracy is indeed possible, our example illustrates the ambiguity of choosing parameters for the artificial gas. This ambiguity is eliminated by using voids.

6.2.2. Shock wave interacting with a spherical void cavity

In this test we demonstrate the ability to simulate the closure of a void cavity by a shock wave. The domain is $(-1.5, -0.5) \times (1.5, 0.5)$. All boundaries are walls. The void bubble is centered at $(0, 0)$ with a radius of $r = 0.3$. The rest of the domain is filled with two regions of ideal gas as follows:

$$\gamma = 1.4, \quad \begin{cases} \rho = 1,\ p = 1 \cdot 10^{-5},\ \mathbf{u} = (0,0) & \text{for} \quad x > -0.5 \\ \rho = 4,\ p = 1.3334,\ \mathbf{u} = (1,0) & \text{elsewhere.} \end{cases}$$

This generates a shock wave, with the front located initially at $x = -0.5$. The shock is moving to the right. The density and velocity fields are displayed in Figs. 30 and 31 – the shock front is visibly deformed after passing through the void bubble. At the time $t = 0.5$ the void is completely closed and the simulation continues in the single-material regime.

6.2.3. Simplified shaped-charge-like problem

This test is a simplified shaped charge problem – we call it shaped-charged-like because it exhibits some of the features of a realistic shaped charge experiment. A simple geometry and the ideal gas equation of state has been used to define the problem, so that interested researchers can easily reproduce our results.

There are two regions filled with ideal gas (see Figure 32 for the material distribution):

■ "high explosive":

$$\gamma = 1.4, \quad \rho = 1, \quad p = 1 \cdot 10^{-7}, \quad \mathbf{u} = (0,0),$$

■ "shell":

$$\gamma = 50, \quad \rho = 10, \quad p = 1 \cdot 10^{-7}, \quad \mathbf{u} = (0,0).$$

The domain occupied by "high explosive" is defined by a polygon with the following vertices:

$$(-1.0, -0.5), (2.5, -0.5), (0.0, 0.0), (2.5, 0.5), (-1.0, 0.5)\,;$$

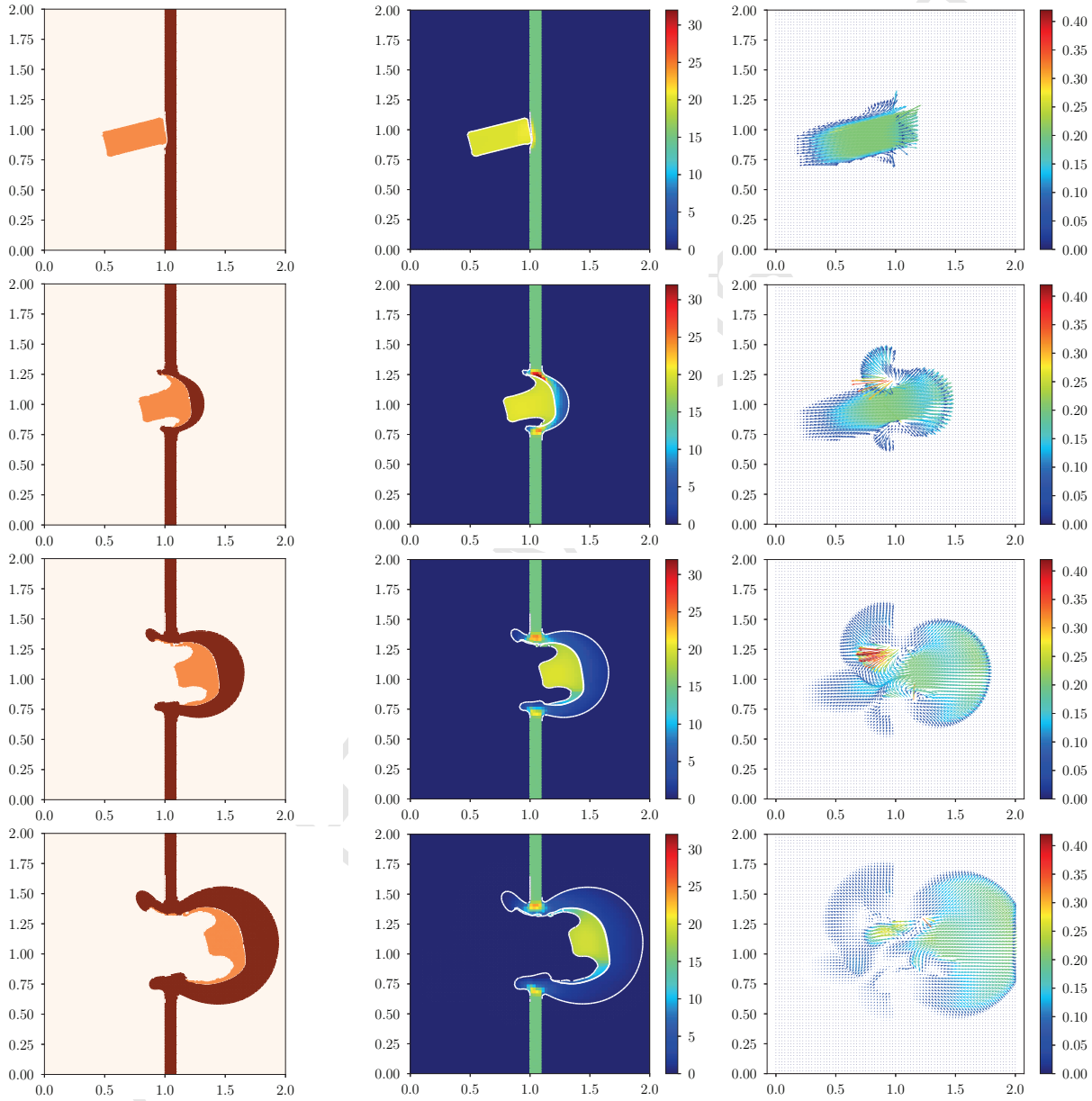

(a) Mat. distribution (b) Density (c) Velocity

Fig. 28: Diagonal projectile-plate impact – results using high gamma/high density artificial gas for various time moments, 80×80 mesh, $t = 1.5, 3, 4.5, 6$ from top to bottom.

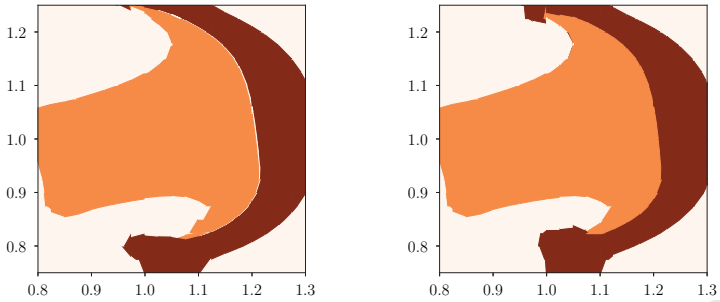

(a) High gamma/high density
The artificial gas is trapped
between real materials

(b) Void treatment
Void completely closed

Fig. 29: Diagonal projectile-plate impact – zoom of the impact zone for 80×80 mesh at $t = 3$.

the shell domain is defined by polygon

$$(2.5, -0.5), (3.0, -0.5), (0.5, 0.0), (3.0, 0.5), (2.5, 0.5), (0.0, 0.0)\,;$$

and the rest is filled with void:

$$(3.0, -0.5), (5.0, -0.5), (5.0, 0.5), (3.0, 0.5), (0.5, 0.0)\,.$$

The boundaries of the domain are walls. Calculations are performed on 20×120 cell mesh.

To imitate the detonator we set a high internal energy, $\varepsilon = 2.5e6$, in the two cells in the "high explosive" that are located adjacent to the left boundary at its center. In Fig.33 we show the isolines for pressure at different time moments.

In Fig.34 we show the shape of the shaped charge (material interfaces) and a color-map for density. The corresponding velocity field is also shown in in Fig.35. We can see that a jet of material has formed which is similar to a shaped charge jet. However, since this is an artificial problem there is no experimental data to compare against.

6.2.4. Unconfined Shaped Charge

In this section we present our first attempt to model a real problem, the so-called unconfined shaped charge. We have loosely followed the description in [23]. The BRL [2] 105 mm unconfined shaped charge is possibly the simplest shaped charge problem available with a good set of experimental data. The geometry and materials in the experiment are shown in Fig. 36 and are taken from [23]. There are only two real materials in the experiment, a high explosive (Composition B) and the copper liner. The high explosive is detonated at the left hand end. The copper liner is then deformed and convergence of the flow in the liner on to the axis produces a jet that can travel at velocities comparable to the detonation velocity of the explosive. The simulation is performed in the two dimensional cylindrical (rz) geometry, using programmed burn to model the detonation of the explosive and with material strength included in the copper liner. All the space around the explosive and liner material is treated as void. An ALE mesh motion strategy is used to increase the resolution in the liner material by applying a weighted equipotential mesh movement strategy. Two simulations have been performed using different multimaterial cell closure models. The first

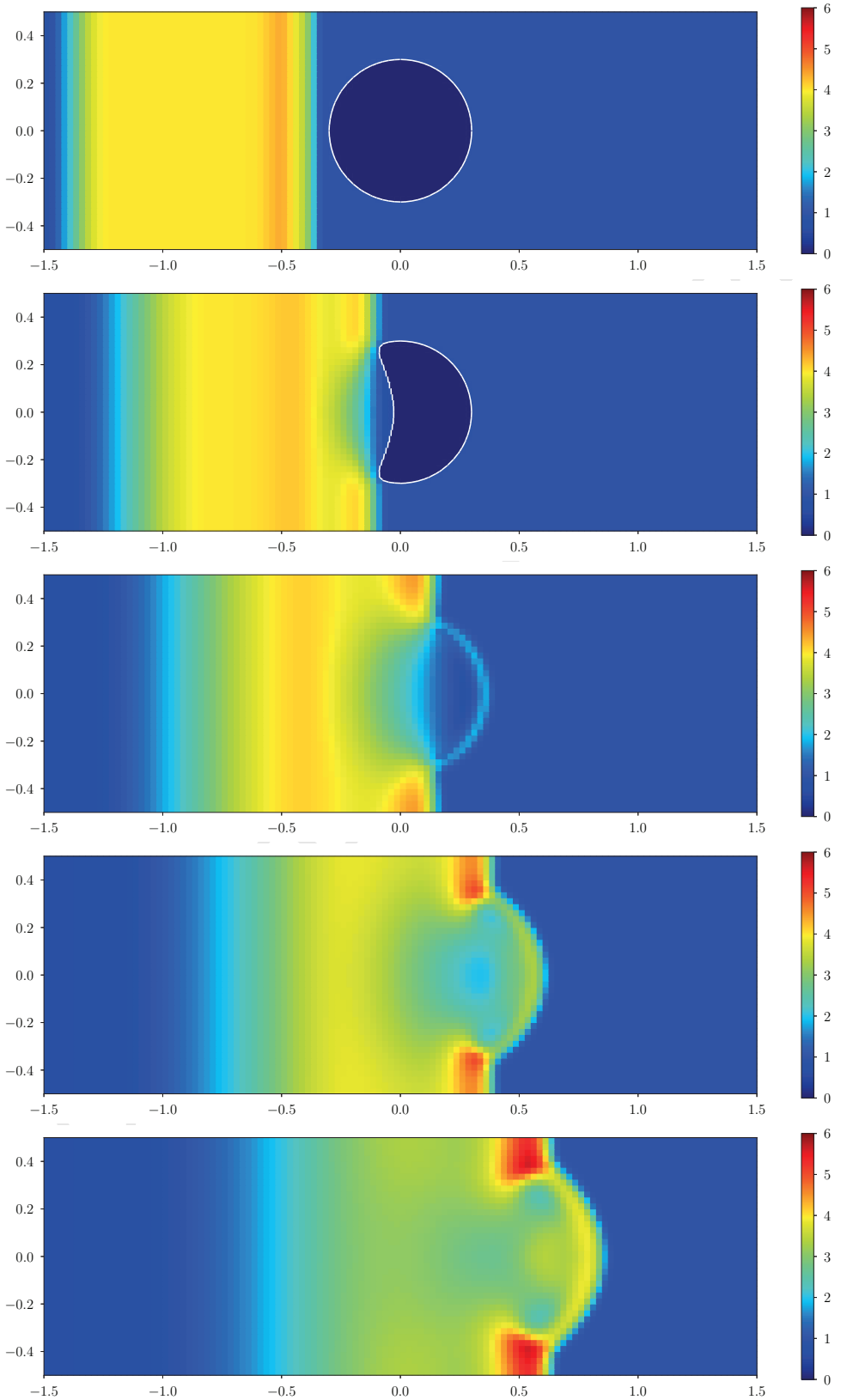

Fig. 30: Shock wave interacting with a spherical void cavity, density profile, 120×40 mesh, $t = 0.1, 0.3, 0.5, 0.7, 0.9$ from top to bottom. On the top two pictures we also show boundary of the void bubble.

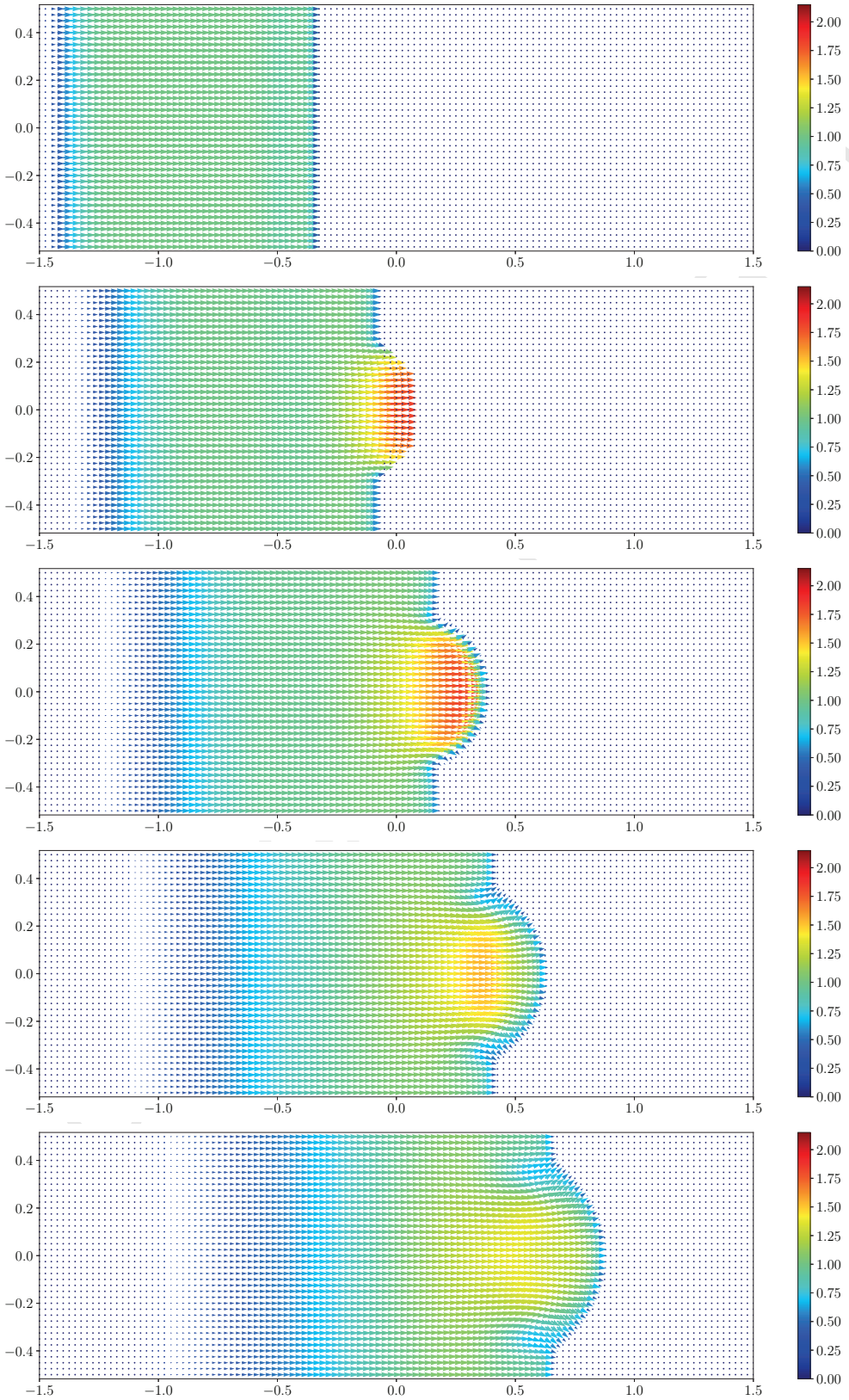

Fig. 31: Shock wave interacting with a spherical void cavity, velocity field, 120×40 mesh, $t = 0.1, 0.3, 0.5, 0.7, 0.9$ from top to bottom.

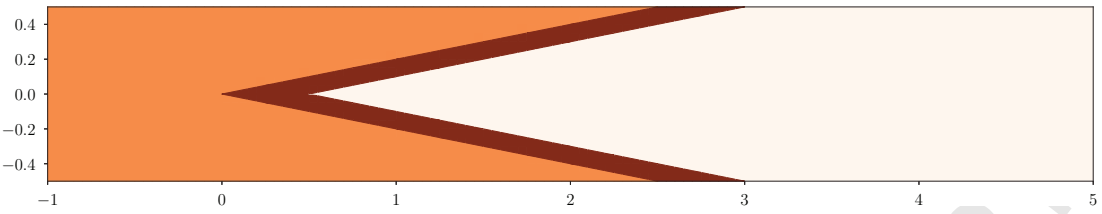

Fig. 32: Simplified shaped charge problem, initial material distribution. ■ "high explosive", ■ "shell", ■ void. 120×20 mesh, $t = 0$.

was performed using the new void closure capability described in this paper. The second was performed using the equal volumetric strain closure model. The intention being to use the two simulations to give an indication of the sensitivity of the shaped charge simulation to the details of the closure model. The initial geometry for the simulation is shown in Fig.37. We do not describe the exact specifications for the equations of state of the materials used because there is no intention to make a quantitative comparison with the experimental data in this paper.

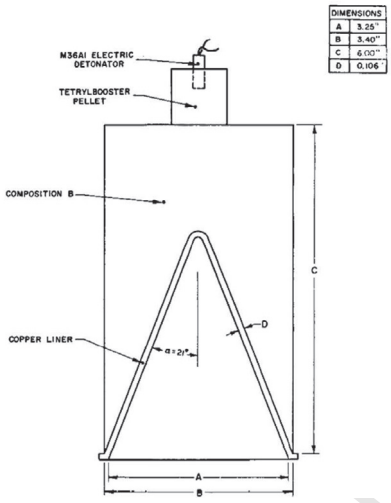

Fig. 36: Drawing of the BRL 105 mm unconfined shaped charge - copied from [23].

In Fig.38 we present the results of our simulation using the equal volumetric strain closure model and in Fig.40 with the new void closure capability for different time moments. A zoom in showing the jet tip and mesh resolution through the jet tip for the equal volumetric strain simulation is given in Fig.39 and for the new void closure capability in Fig.41. The jet tip produced by the new void closure treatment is flatter and blunter than that obtained with equal volumetric strain.

The numerical results are presented only to show that the void closure algorithm described in this paper can be applied to real problems with real materials, including solids. However, we would like to mention that both the sets of results we present are in reasonable agreement with the results presented in [23]. The main differences observed between these three sets of results is in the shape of the jet tip. The new void closure model we have described in this paper produces the most blunt jet tip and Pagosa code, [23], simulation produces the sharpest jet tip, while the equal volumetric strain simulation lies somewhere between the other two. This suggests the structure of the shaped charge jet tip is sensitive to the details of the multimaterial cell closure model used. A blunter jet tip such as that produced by the new void closure model is considered to be more physically justifiable and what is usually observed experimentally as can be seen in [25].

7. Conclusions

In this paper we have extended the constrained optimization-based framework for the interface-aware sub-scale dynamics [3] closure model to support multimaterial cells containing void with the ability to close.

The IA-SSD closure model for the Lagrangian stage of ALE consists of two stages. At the first, *bulk*, stage

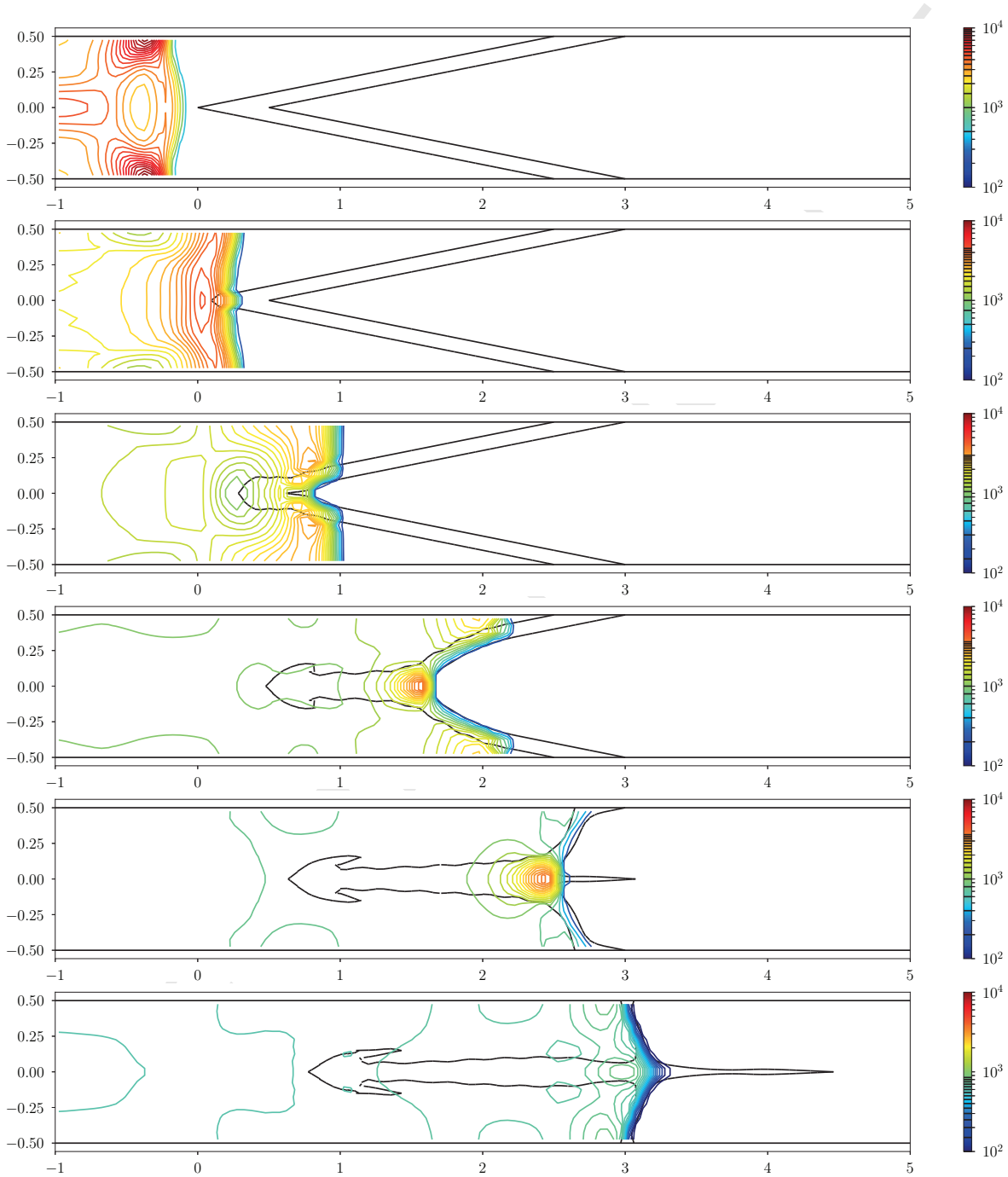

Fig. 33: Simplified shaped-charge-like problem, isolines of pressure, $t = 5, 10, 20, 40, 60, 80$ from top to bottom.

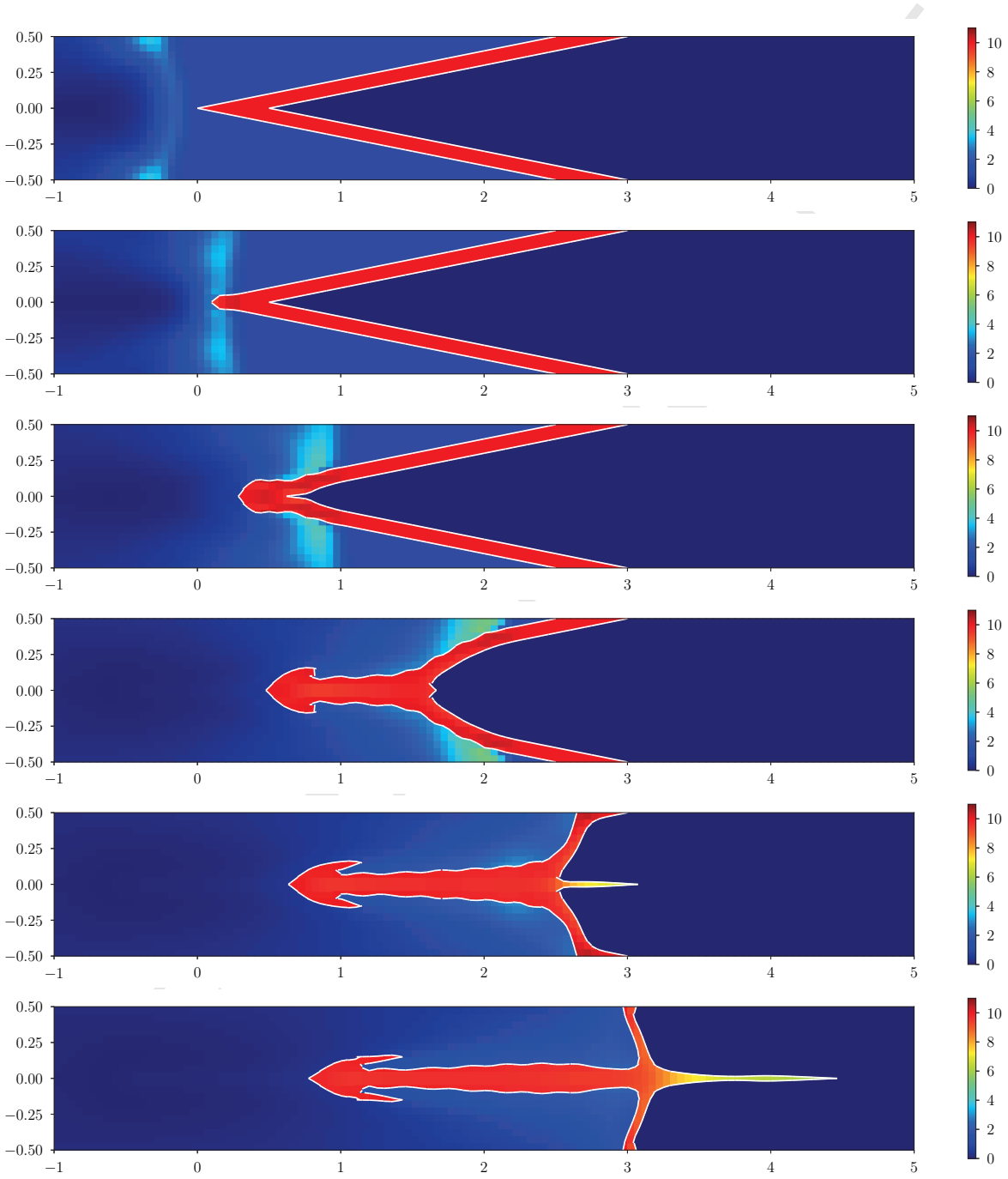

Fig. 34: Simplified shaped-charge-like problem, material interfaces and a density color-map, $t = 5, 10, 20, 40, 60, 80$ from top to bottom.

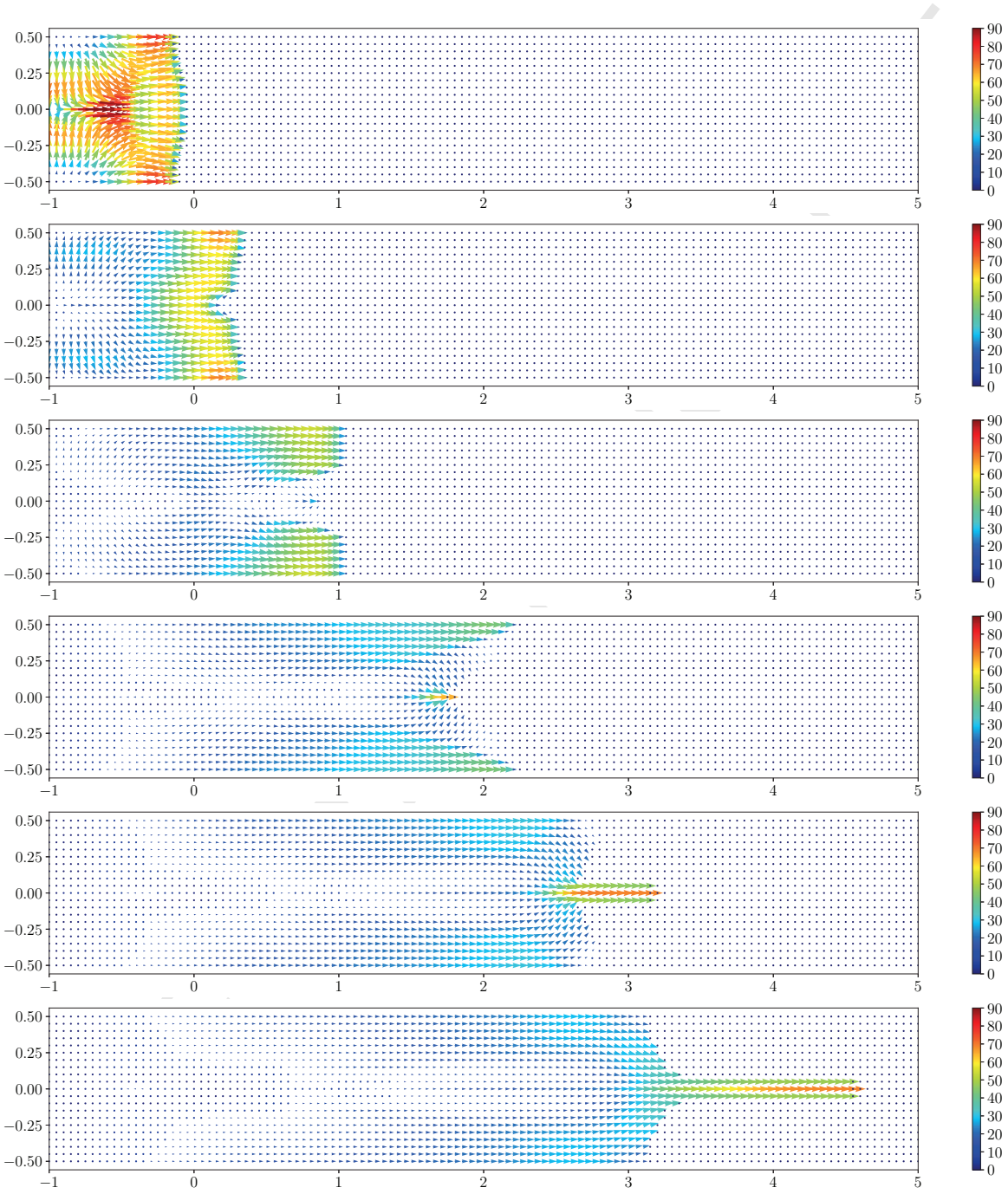

Fig. 35: Simplified shaped-charge-like problem, velocity field, $t = 5, 10, 20, 40, 60, 80$ from top to bottom.

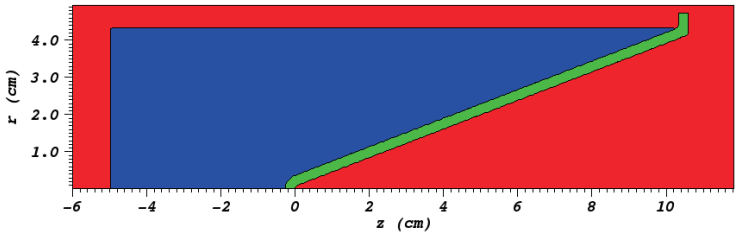

Fig. 37: Initial configuration for the shaped charge problem. ■ high-explosive, ■ copper liner, ■ void.

we use the the equal compressibility model. Void cannot close at this stage. During the second, *sub-scale*, stage, the interactions of the materials inside the multimaterial cell are taken into account. Each material including void interacts in a pair-wise fashion with the materials with which it has a common boundary.

The pair-wise interactions of the real materials and void are based on the solution of the acoustic Riemann problem between each pair and are limited using physically justified constraints. The constraints applied are: positivity of volume for real materials, non-negativity of the volume of void, positivity of internal energy and controlled rate of pressure relaxation. The volume of the void can be zero as a result of the sub-scale stage, which indicates that the void has closed. To determine the values of the limiter coefficients, a constrained-optimization framework is employed using a quadratic objective function with linear constraints.

We have demonstrated that the new void closure model can be successfully used to simulate problems including; two-body impacts, collapse of a cavity containing a vacuum and shock-driven expansion into vacuum. Moreover, the new method eliminates the ambiguity of choosing parameters for an artificial gas material used to mock up a vacuum, which can often lead to a compromise between robustness, efficiency and accuracy. This is shown on various 1D and 2D numerical examples.

In the future we plan to describe our algorithm for the case of solid-void interactions and present a quantitative comparison of our numerical results with experimental data for problems like shaped-charges. We also plan to introduce a procedure for void opening and explore phenomena such as multimaterial sliding and friction.

8. Acknowledgments

This work was performed under the auspices of the National Nuclear Security Administration of the US Department of Energy at Los Alamos National Laboratory under Contract No. DE-AC52-06NA25396. The authors gratefully acknowledge the partial support of the US Department of Energy Office of Science Advanced Scientific Computing Research (ASCR) Program in Applied Mathematics Research and the partial support of the US Department of Energy National Nuclear Security Administration Advanced Simulation and Computing (ASC) Program. This work was partially supported by the Czech Technical University grant SGS16/247/OHK4/3T/14, the Czech Science Foundation project 18-20962S and the Czech Ministry of Education project RVO68407700.

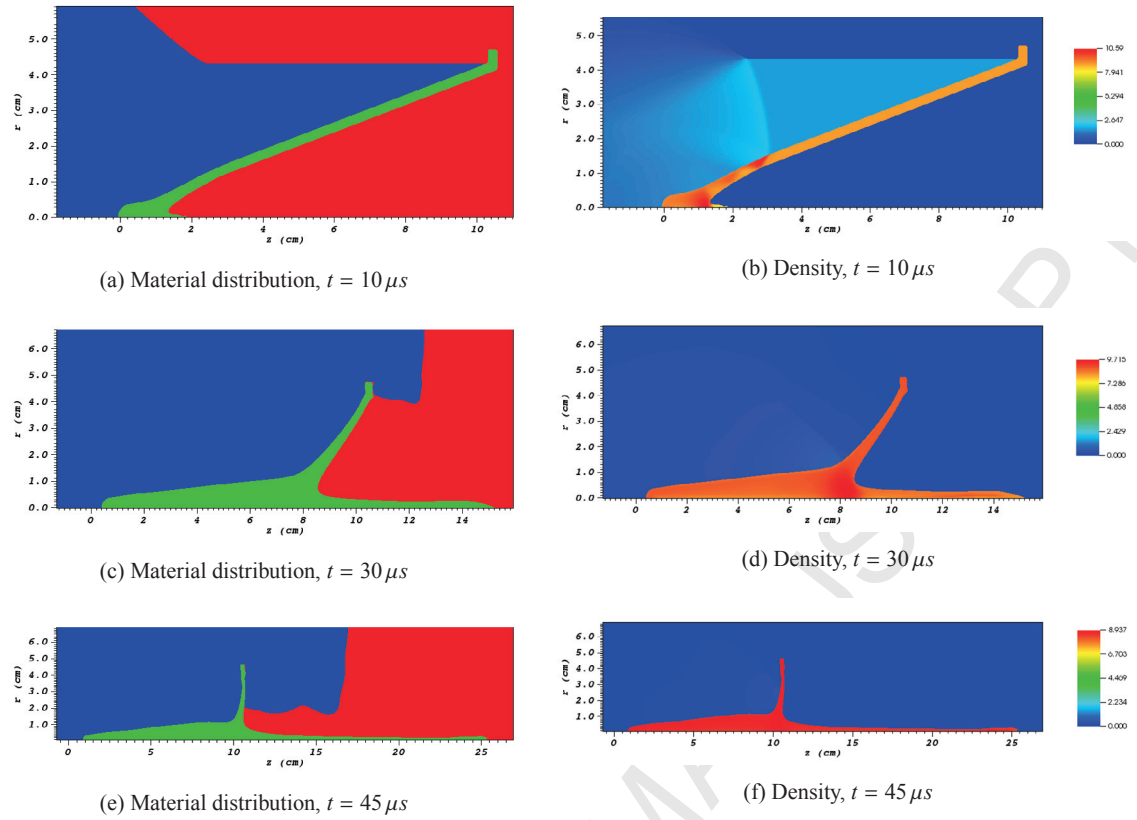

(a) Material distribution, $t = 10\,\mu s$

(b) Density, $t = 10\,\mu s$

(c) Material distribution, $t = 30\,\mu s$

(d) Density, $t = 30\,\mu s$

(e) Material distribution, $t = 45\,\mu s$

(f) Density, $t = 45\,\mu s$

Fig. 38: Unconfined BRL shaped-charge example, equal volumetric strain model

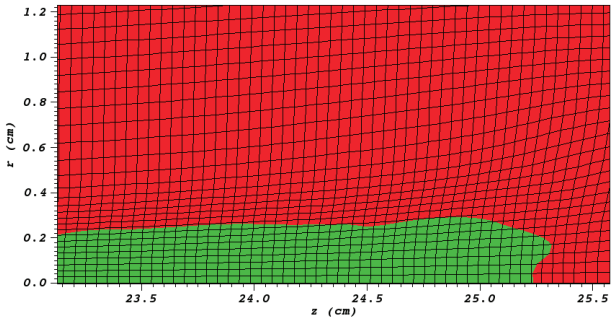

Fig. 39: Unconfined BRL shaped-charge example, equal volumetric strain model. Material distribution, zoom at the tip shape, $t = 45\,\mu s$

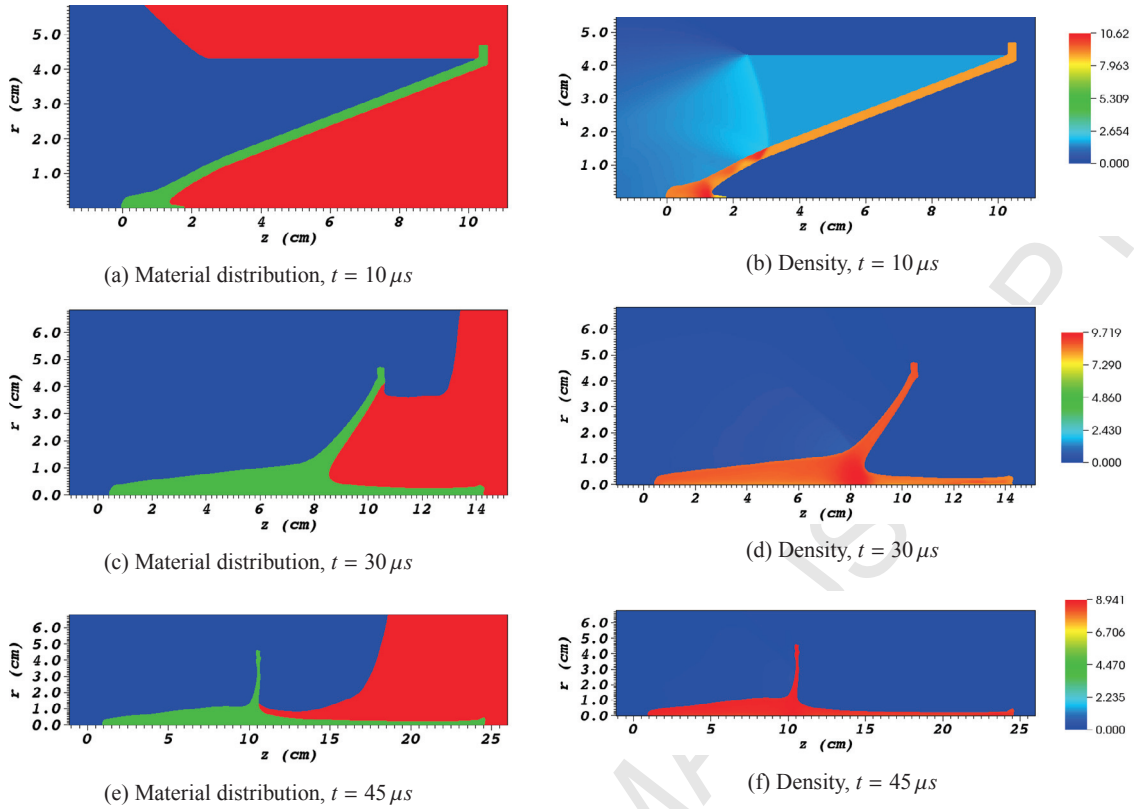

(a) Material distribution, $t = 10\,\mu s$

(b) Density, $t = 10\,\mu s$

(c) Material distribution, $t = 30\,\mu s$

(d) Density, $t = 30\,\mu s$

(e) Material distribution, $t = 45\,\mu s$

(f) Density, $t = 45\,\mu s$

Fig. 40: Unconfined BRL shaped-charge example, IASSD model with void closure.

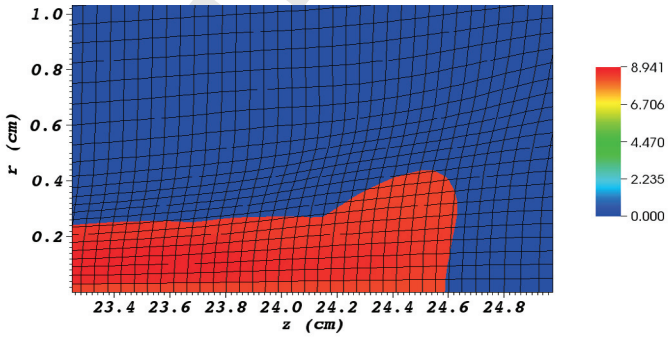

Fig. 41: Unconfined BRL shaped-charge example, IASSD model with void closure. Density, zoom at the tip shape, $t = 45\,\mu s$.

The authors thank D. Burton. A. Harrison, J. Fung, T. Canfield, M. Francois, D. Youngs, M. Kucharik, R. Hill, M. Dumbser, N. Morgan, R. Liska, D. Benson, Y. Yanilkin, Y. Bondarenko, B. Wendroff, J. Grove, B. Despres, R. Loubere, P. Vachal, T. Masser, E. Dendy, B. Rider, D. Miller, R. Abgrall, for many useful discussion over the years.

Special thanks to E. Kikinzon for allowing us to use X-MOF interface reconstruction code.

References

[1] H. Ahn, M. Shashkov, Multi-material interface reconstruction on generalized polyhedral meshes, J. Comput. Phys. 226 (2007) 2096–2132.
[2] F. Allison and R. Vitali, An Application of the Jet Formation Theory to a 105mm Shaped Charge, Ballistics Research Laboratory, Report No. 1165 (March 1962).
[3] A. Barlow, R. Hill, M. Shashkov, Constrained optimization framework for interface-aware sub-scale dynamics closure model for multimaterial cells in Lagrangian and arbitrary Lagrangian Eulerian hydrodynamics, J. Comput. Phys., 276 (2014), pp. 92-135
[4] A. J. Barlow, P.-H. Maire, W.J. Rider, R.N. Rieben, and M.J Shashkov, Arbitrary Lagrangian-Eulerian Methods for Modeling High-speed Compressible Multimaterial Flows, J. Comput. Phys., 322 (C), (2016) 603–665.

[5] A. Barlow, M. Klima, M. Shashkov, Constrained optimization framework for interface-aware sub-scale dynamics closure models with voids for multimaterial cells in Lagrangian hydrodynamics, Technical Report of Los Alamos National Laboratory, LA-UR-17-28814. Available at https://www.researchgate.net/publication/321136813
[6] D. Benson, Computational methods in Lagrangian and Eulerian hydrocodes, Journal Computer Methods in Applied Mechanics and Engineering 99 (2–3) (1992) 235–394.
[7] E. Caramana, D. Burton, J. Shashkov, M, P. Whalen, The construction of compatible hydrodynamics algorithms utilizing conservation of total energy, J. Comput. Phys. 146 (1998) 227–262.

[8] R.A. Carson and O. Sahni, Effect of channel geometry on blast overpressure attenuation for a large caliber cannon, In Proceedings of the 28th International Symposium on Ballistics, Atlanta, Georgia, USA, 22-26 September, 2014, Volume 2, Eds. R.G. Amesa and R.D. Boeka, pp. 1711–1721, DEStech Publications,Inc. 2014.

[9] R.B. DeBar, Fundamentals of the KRAKEN Code, Report of Lawrence Livermore Laboratory, UCID-17366, (1974). Available at https://www.osti.gov/scitech/biblio/7227630
[10] V. Dyadechko, M. Shashkov, Reconstruction of multi-material interfaces from moment data, J. Comput. Phys. 227 (2008) 5361–5384.
[11] C. Hirt, A. Amsden, J. J. L. Cook, An arbitrary Lagrangian- Eulerian computing method for all flow speeds, Journal of Computational Physics 14 (3) (1974) 227–253.

[12] X.Y. Hu and B.C. Khoo, Kinetic energy fix for low internal energy flows, J. Comput. Phys. 193 (2003) 243–259.
[13] E. Kikinzon, Yu. Kuznetsov, K. Lipnikov and M. Shashkov, Approximate static condensation algorithm for solving multi-material diffusion problems on meshes non-aligned with material interfaces, J. Comput. Phys. 347 (2017) 416–436.
[14] M. Kuchařík, M. Shashkov, Conservative multi-material remap for staggered multi-material arbitrary Lagrangian-Eulerian methods, J. Comput. Phys. 258 (2014) 268–304.
[15] C.-D. Munz, A tracking method for gas flow into vacuum based on the vacuum Riemann problem, Math. Meth. Appl. Sc. 17 (1994) 597-612.
[16] J. Nocedal, S. Wright, Numerical Optimization, Springer, 1999.
[17] W.J. Rider, Void's Unphysical Response In Hydrocodes, Presentation at Nuclear Explosives Code Development Conference held October 20-24, 2014 in Los Alamos, NM, SAND2014-18762PE, Available at https://www.osti.gov/scitech/biblio/1241862

[18] W. Rider, A. Robinson et al. Algorithm Developments in ALEGRA Guided by Testing, Presentation at the conference on Numerical methods for multi-material fluid flows, Czech Technical University, Prague, Czech Republic, September 10 - 14, 2007. Available at www.cs.sandia.gov/ALEGRA/Presentations/Prague2007AlegraAlgorithmTesting.pdf

[19] A.C. Robinson, O.E. Strack, et al, ALEGRA Update: Modernization and Resilience Progress, Report of Sandia National Laboratory, SAND2013-7960C 477209. Available at https://www.osti.gov/scitech/biblio/1115141

[20] A.C. Robinson, J.H.J. Niederhaus, V.G.Weirs and E. Love, Arbitrary Lagrangian-Eulerian 3D ideal MHD algorithms, Int. J. Numer. Meth. Fluids, 65 (2011), pp.1438–1450.
[21] K. Schittowski, Ql: A Fortran code for convex quadratic programming - user's guide, Tech. rep., University of Bayreuth, Dept. of Computer Science, `www.klaus-schittkowski.de/software.htm` (2011).
[22] E.F. Toro, Riemann solvers and numerical methods for fluid dynamics. Practical introduction. Second edition, Springer, 1999.
[23] W.N. Weseloh, PAGOSA Sample Problem: Unconfined Shaped Charge LA-UR-16-20590, 2016.
[24] J. Zukas, Introduction to Hydrocodes, Studies in Applied Mechanics - 49, Elsevier, 2004.
[25] J. Zukas, W. P. Walters, Fundamentals of Shaped Charges, Wiley Interscience, 1989.